JℳM PAPERS

Putting the micro into the macro: a molecularly augmented hydrodynamic model of dynamic wetting applied to flow instabilities during forced dewetting

J.S. Keeler[1],†, T.D. Blake[2],†, D.A. Lockerby[3],† and J.E. Sprittles[4],†

[1]School of Mathematics, University of East Anglia, Norwich NR4 7TJ, UK

[2]Independent Consultant

[3]School of Engineering, University of Warwick, Coventry CV4 7AL, UK

[4]Mathematics Institute, University of Warwick, Coventry CV4 7AL, UK

We report a molecularly augmented continuum-based computational model of dynamic wetting and apply it to the displacement of an externally driven liquid plug between two partially wetted parallel plates. The results closely follow those obtained in a recent molecular dynamics (MD) study of the same problem (Fernández-Toledano *et al.*, *J. Colloid Interface Sci.*, vol. 587, 2021, pp. 311–323), which we use as a benchmark. We are able to interpret the maximum speed of dewetting U^*_{crit} as a fold bifurcation in the steady phase diagram and show that its dependence on the true contact angle θ_{cl} is quantitatively similar to that found using MD. A key feature of the model is that the contact angle is dependent on the speed of the contact line, with θ_{cl} emerging as part of the solution. The model enables us to study the formation of a thin film at dewetting speeds $U^* > U^*_{crit}$ across a range of length scales, including those that are computationally prohibitive to MD simulations. We show that the thickness of the film scales linearly with the channel width and is only weakly dependent on the capillary number. This work provides a link between matched asymptotic techniques (valid for larger geometries) and MD simulations (valid for smaller geometries). In addition, we find that the apparent angle, the experimentally visible contact angle at the fold bifurcation, is not zero. This is in contrast to the prediction of conventional treatments based on the lubrication model of flow near the contact line, but consistent with experiment.

† Email addresses for correspondence: j.keeler@uea.ac.uk, terrydblake@btinternet.com, duncan.lockerby@warwick.ac.uk, j.e.sprittles@warwick.ac.uk

J.S. Keeler, T.D. Blake, D.A. Lockerby and J.E. Sprittles

Key words: contact lines, liquid bridges, thin films

---

1. Introduction

Dynamic wetting, the process by which a liquid wets a solid surface, is an important phenomenon that underpins a wide range of both industrial and natural processes, including microfluidics (Stone, Stroock & Ajdari 2004), liquid coating and printing operations (Weinstein & Ruschak 2004), petroleum recovery (Gerritsen & Durlofsky 2005), plant protection (Papierowska *et al.* 2018), ground water hydrology (Beatty & Smith 2010) and biological processes (Barthlott, Mail & Neinhuis 2016). As such, it presents a multiscale problem. Whilst its origin is at the microscopic scale of the moving contact line, it influences outcomes at very much larger scales. However, despite this importance, and consequent research over many decades, there remain fundamental questions about the physics involved and, in particular, the role of solid–liquid interactions at the moving contact line (Andreotti & Snoeijer 2020; Afkhami, Gambaryan-Roisman & Pismen 2020; Semenov *et al.* 2011). One such difficulty is the determination of the slip length from experiments. In this paper we develop a continuum model that does not require the slip length, which is difficult to measure experimentally, to be specified. The only parameter that we require is the width of the three-phase zone (TPZ), which can be easily extracted from molecular dynamics (MD) simulations and an experimental determination of the contact line friction for system-specific studies. MD simulations are prohibitively expensive when the physical system size is large, but by simply changing a single parameter in our model we are able to probe the dynamics of larger systems which are beyond the capabilities of MD.

In wetting studies solid–liquid interactions are usually quantified in terms of the angle of contact between the liquid and the solid, and its proper description has attracted much attention (De Gennes 1985; Blake 2006; Shikhmurzaev 2007; Andreotti & Snoeijer 2020). From hydrostatic and hydrodynamic perspectives, this boundary condition is crucial, as it dictates the shape of the liquid volume. The way it changes in response to movement of the contact line across the solid surface is, therefore, fundamental to our ability to predict wetting outcomes. Nevertheless, the description of the true contact angle at a moving contact line remains hotly debated (Andreotti & Snoeijer 2020; Afkhami *et al.* 2020; Semenov *et al.* 2011).

In continuum models the true contact angle, measured by the tangent of the interface at the solid (see figure 1), has to be specified in order to solve the governing equations and is usually considered to be constant and equal to the equilibrium value. The observed dynamics of the apparent contact angle (i.e. the one seen experimentally Wilson *et al.* 2006) is attributed to the 'viscous bending' of the interface: this is the so-called 'hydrodynamic' or Cox–Voinov formulation (Cox 1986; Voinov 1976). However, according to the molecular-kinetic theory (MKT) of wetting (Blake & Haynes 1967; Blake 1993) and the interface formation model (Shikhmurzaev 2007), the true contact angle varies and is dependent on the velocity of the contact line.

Here, we will show that viscous bending alone is insufficient to capture the effects seen in molecular simulations, where the velocity dependence of the actual contact angle is observed. Therefore, we develop a new combined approach based on the Navier–Stokes continuum paradigm combined with the MKT (whose formulation is far simpler than the interface formation model, despite the latter's attractive features) and focus it on the canonical dynamic wetting problem of a liquid plug propagating through a channel.
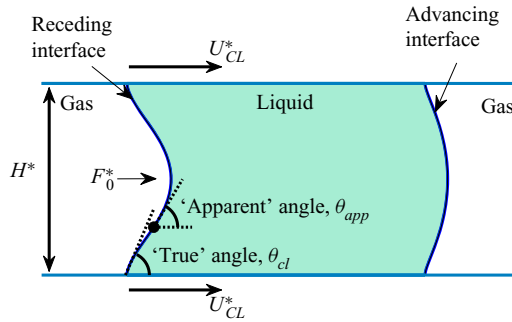
Figure 1. Schematic of a liquid plug between two plates subject to an external forcing F_0^*. The angle that the receding contact line makes with the plate is the true angle, denoted θ_{cl}. See figure 6 for a more detailed schematic of the angle measurements.

In particular, in order to allow for unambiguous comparisons to the results of MD on a comparable system, we identify a critical speed at which a flow bifurcation occurs and a thin film is formed.

The study of dynamic wetting using molecular simulations has a long history, see review articles De Coninck & Blake (2008) and Koplik & Banavar (1995); but here we focus on a recent paper, Fernández-Toledano *et al.* (2021), that examines both wetting transitions and the behaviour of the contact angle. In this study large-scale MD is utilised to explore the steady displacement of a water-like liquid plug between two molecularly smooth solid plates under the influence of an external driving force F_0^* (see figure 1 for the geometry). The study used a coarse-grained model of water and an atomistic Lennard–Jones model for the solid plates. The general behaviour observed as F_0^* was increased and, hence, the liquid plug's speed was raised, is depicted in figure 2. Notably, it was reported that both the 'true', dynamic contact angle at the contact line, θ_{cl}, and a larger-scale 'apparent' angle, θ_{app}, are dependent on the contact line velocity U_{cl}^* for the receding and advancing interfaces. Henceforth, unless otherwise stated, when we refer to a 'contact angle' we mean the 'true' contact angle. We also note that quantities labelled with an asterisk correspond to dimensional physical quantities and those without to dimensionless quantities.

In the MD study, the apparent angle was measured at the system scale by a method that mimics typical measurements of it in macroscopic experiments, where the precise details of the true contact angle's dynamics remain hidden, as they occur on such small length scales (Hoffman 1975; Dussan 1979; Blake 2006). By varying the solid–liquid affinity (i.e. the solid's wettability), it was possible to investigate the influence of the equilibrium contact angle θ_0 on the results. For all θ_0, θ_{cl} was found to be velocity dependent in a manner consistent with the MKT of dynamic wetting (Blake & Haynes 1967; Blake 1993). However, θ_{app} diverged from θ_{cl} as F_0^* was increased, especially at the receding contact line (RCL), in a way that closely followed the Voinov equation (Voinov 1976)

$$\theta_{app}^3 = \theta_{cl}^3 + 9\,Ca\log(L^*/L_m^*), \tag{1.1}$$

where $Ca = \mu^* U_{cl}^*/\gamma^*$ is the capillary number based on the contact line speed U_{cl}^*, dynamic viscosity μ^* and surface tension γ^*, and L^* and L_m^* are suitably chosen macroscopic and microscopic length scales. For each θ_0, there was a critical RCL velocity U_{crit}^* and contact angle θ_{crit} at which θ_{app} became small and the receding meniscus deposited a liquid film on the plates. This value could then be used in (1.1), assuming $\theta_{app} \approx 0$, to fix L^*/L_m^* and, hence, reliably predict θ_{cl} at both the ACL and RCL.
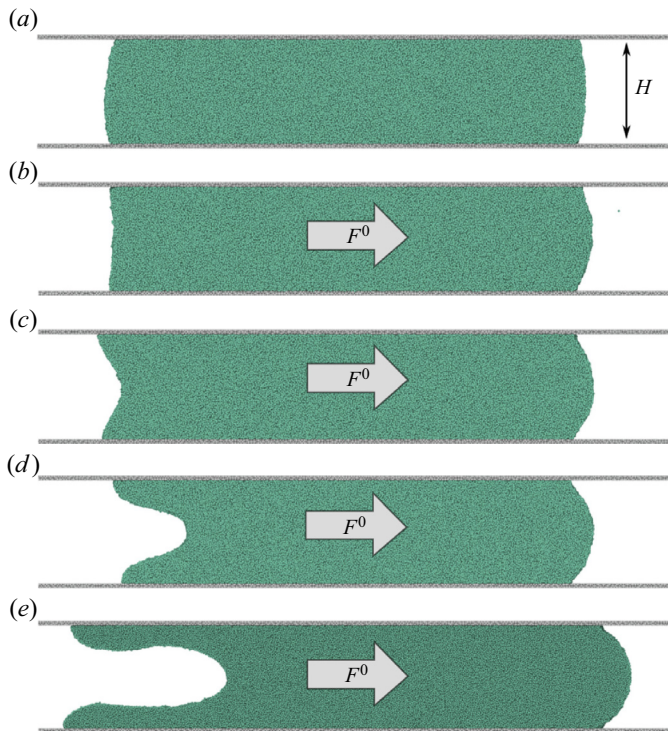
Figure 2. Figure reprinted from Fernández-Toledano, Blake & De Coninck (2021), with permission from Elsevier. Panels (*a–e*) show the liquid plug as the force F_0^* (in the article asterisks were not used to denote dimensional quantities) becomes successively larger and eventually exceeds the critical value (panels *d,e*) where a thin film begins to develop. In this MD simulation the external phase is a vacuum.

This result is significant, as θ_{cl} is not usually experimentally accessible and the fact that it varies with U_{cl}^* poses questions for hydrodynamic interpretations of dynamic wetting. The result also shows that the critical condition for film deposition encodes crucial information about the hydrodynamics.

The existence of a critical wetting speed has been investigated thoroughly using hydrodynamic models in a range of geometries, including those associated with coating flows (Kumar 2015) and plate withdrawal (Snoeijer *et al.* 2008), among others. In Keeler *et al.* (2021) both receding and advancing contact line (ACL) problems were investigated for a coating flow and the stability of the solutions near the critical speed was quantified using a dynamical systems method. Here, our focus will be on the RCL, as this is where the first bifurcation will occur. Previous studies have shown that as Ca increases, the RCL will attain a steady state provided $Ca < Ca_{crit}$, where Ca_{crit} is a critical capillary number that is a function, at the very least, of θ_{cl}, the slip length and the viscosity ratio of the liquid and gas phases (Cox 1986; Eggers 2004; Snoeijer *et al.* 2006, 2007; Keeler *et al.* 2021), but, if $Ca > Ca_{crit}$, a thin film develops with thickness dependent on Ca (Snoeijer *et al.* 2006; Keeler *et al.* 2021). Using a lubrication model, Ca_{crit} can be approximated when the slip length is small relative to the film height (Eggers 2005), by considering a small-Ca asymptotic analysis and using the key assumption that $\theta_{app} = 0$ at the critical point. However, in a nano-geometry, as considered here, we will see that this assumption is not valid and the resulting small-Ca asymptotic analysis does not extend to this regime.

In this paper we will develop a hydrodynamic model based on the Navier–Stokes paradigm to calculate steady states and transient behaviour of the liquid plug scenario considered in Fernández-Toledano *et al.* (2021). An essential aspect of this model is that the true angle, θ_{cl}, has to be specified at the junction of the liquid, gas and solid phases. In many previous studies where a Navier–Stokes model is used (see, e.g. Sprittles & Shikhmurzaev 2012; Kamal *et al.* 2019; Liu, Carvalho & Kumar 2019; Vandre, Carvalho & Kumar 2012, 2013; Liu *et al.* 2016*a*,*b*; Liu, Carvalho & Kumar 2017) θ_{cl} is assumed to be constant and, in others, whilst the angle varies this is to account for sub-grid-scale variations in the apparent angle, rather than variation of θ_{cl} (Sui, Ding & Spelt 2014).

Motivated by the results of Fernández-Toledano *et al.* (2021) we relax this assumption and adopt a model that determines θ_{cl} as a function of *Ca* and the static contact angle θ_0 based on the MKT. Notably, the model remains hydrodynamic throughout, in contrast, for example, to Hadjiconstantinou (1999), and the molecular augmentation comes entirely through the contact angle formula.

The approach of using molecular simulations to develop a macroscopic framework for dynamic wetting builds on a number of influential works in this area. Notably, in Qian, Wang & Sheng (2003) molecular simulations revealed the existence of the 'uncompensated Young stress' in the contact line region that led the authors to derive a 'generalized Navier boundary condition' that fits into a Cahn–Hilliard computational framework where the molecular-scale diffuse nature of the interface is resolved. In Ren & E (2007) a careful analysis of contact line force contributions in MD was also considered, but within the sharp-interface regime this led the authors to propose a hydrodynamic model similar to the one considered here, Navier slip and the use of the MKT to account for the contact line region's dynamics. This work was extended in Ren, Hu & E (2010) to account for complete wetting states. Again, motivated by MD, more recent approaches have even considered modifications to impermeability of the solid–liquid interface (Lukyanov & Pryer 2017) that change the flow kinematics near the contact line. Notably, such models subsequently became the basis of macroscopic CFD-type codes for wetting, e.g. Xu & Ren (2014) and Yue & Feng (2011). Previous articles considering MD have, understandably, focused on steady states where the advantages of time averaging of MD obtained quantities can be exploited. Here, we expand on these articles to focus on flow instabilities at the RCL, which is known to be a sensitive test for dynamic wetting theories (Snoeijer & Andreotti 2013).

Macroscopic models previously proposed, including, in particular, those using the MKT (Reddy, Schunk & Bonnecaze 2005; Dodds, Carvalho & Kumar 2012), often consider that the static contact angle, θ_0, and slip length are independent parameters. Motivated again by Blake *et al.* (2015) and Fernández-Toledano, Blake & De Coninck (2020*b*), we will make use of a correlation between slip length and θ_0 that reduces the number of parameters that are required. This correlation is based on an assumption, borne out by MD simulations, that the mechanism of slip between a liquid and a solid is the same across all parts of the solid–liquid interface, including the contact line.

The paper is structured as follows. In §2 we describe the system of equations used to model the liquid plug based on the Navier–Stokes equations. In addition to the Navier–Stokes equations, in §3 we discuss asymptotic results, based on a quasi-parallel (QP) lubrication approach adapted from Eggers (2005), that will be relevant here. By calculating numerical solutions of the governing equations using a finite-element framework, we will then show in §4 that the critical speed of wetting for the entire liquid plug is dependent on the RCL and not influenced by the ACL. We will also discuss the method for calculating the apparent angle. Next, in §5 we will show how

augmenting the Navier–Stokes equations with an MKT variable-angle (VA) constraint predicts the existence of a critical Ca, and that as the wettability is varied the values of Ca_{crit} match favourably with the MD data in Fernández-Toledano *et al.* (2021), in contrast to the predictions of the fixed-angle model. In addition, we demonstrate how θ_{cl} and θ_{app} vary with the slip length and, thus, provide an estimate of L^*/L_m^* for the liquid plug system, which shows excellent agreement with the MD simulations. Furthermore, in § 6 we examine time-dependent behaviour when $Ca > Ca_{crit}$ so that a thin film develops, whose height obeys a Landau–Levich law. Finally, in § 7, having validated the system in the liquid nano-plug geometry, we exploit our computational framework to explore larger-scale systems, which are beyond the scope of MD simulations. By examining systems where the physical size is orders of magnitude larger than the nano-channel studied in Fernández-Toledano *et al.* (2021), we will show that the dimensionless thickness of the film remains constant for a fixed Ca.

2. Molecular-augmented hydrodynamic model

We will now describe the hydrodynamic model. We shall discuss the full system, based on the Navier–Stokes equations and then describe two different system formulations, the pressure-driven problem and the force-driven problem, as well as the numerical method and the different computational domains.

2.1. *Fully nonlinear system*

To mimic the molecular simulations, we model the liquid-bridge system as a two-dimensional flow between two parallel plates as illustrated in figure 1 and detailed in figure 3(*a*). A finite liquid region fills the channel bounded by two rigid plates that are separated by a distance H^*. We solve in a frame of reference that moves with the plug, with the walls moving with velocity U_{wall}^*. The exact formulation depends on the domain and problem that we consider (i.e. pressure-driven or body-force driven), details of which we discuss later. We non-dimensionalise all lengths using the half-height, $H^*/2$, all velocities using U_{wall}^*, all pressures by $\mu^* U_{wall}^*/(H^*/2)$, all time scales by $(H^*/2)/U_{wall}^*$ and the body force by $\mu^* U_{wall}^*/(H^*/2)^2$. The physical values from the nano-channel geometry of Fernández-Toledano *et al.* (2021) are $H^* = 20.2$ nm, $\mu^* = 0.37$ mPa s^{-1}, $\rho^* = 997$ kg m^{-3} and $\gamma^* = 66 \times 10^{-3}$ Nm^{-1}. The physical velocity U_{wall}^* ranges from 1 to 10^2 m s^{-1}. As in other studies (Sprittles & Shikhmurzaev 2011*b*,*a*; Vandre *et al.* 2012; Sprittles & Shikhmurzaev 2013; Vandre *et al.* 2013; Liu *et al.* 2016*a*,*b*, 2017, 2019), we apply the Stokes-flow approximation, (2.1)–(2.2), so that the Reynolds number, $\rho^* U_{wall}^* H^*/\mu^*$, is assumed to be negligibly small; simple estimates confirm that this is appropriate for the nano-system. We neglect the influence of gravity and assume that the gas phase can be modelled as a vacuum (as seen in figure 2, there are no molecules in the gas phase). A typical computational domain is shown in figure 3(*a*). On the moving wall ($y = 0$) we apply a Navier-slip condition, (2.3), and, therefore, introduce a dimensionless slip length, λ. The MD simulations in figure 2 indicate the flow is symmetric around the centreline of the channel and, hence, we introduce a symmetry wall at $y = 1$, labelled Γ_2, where we set the vertical component of velocity to be zero, apply zero tangential stress and let the horizontal velocity be determined as part of the solution. As well as the fluid velocity field, $\boldsymbol{u}(t, \boldsymbol{x})$, and pressure, $p(t, \boldsymbol{x})$, which depend on the dimensionless time, t, and the position, $\boldsymbol{x}$ of the interfaces, denoted $\boldsymbol{R}_{adv} = (x_a(t, s), y_a(t, s))$ and $\boldsymbol{R}_{rec} = (x_r(t, s), y_r(t, s))$, respectively, are also unknowns in the problem and functions of t and

(*a*)

Half liquid-plug domain

(*b*)

Receding contact line
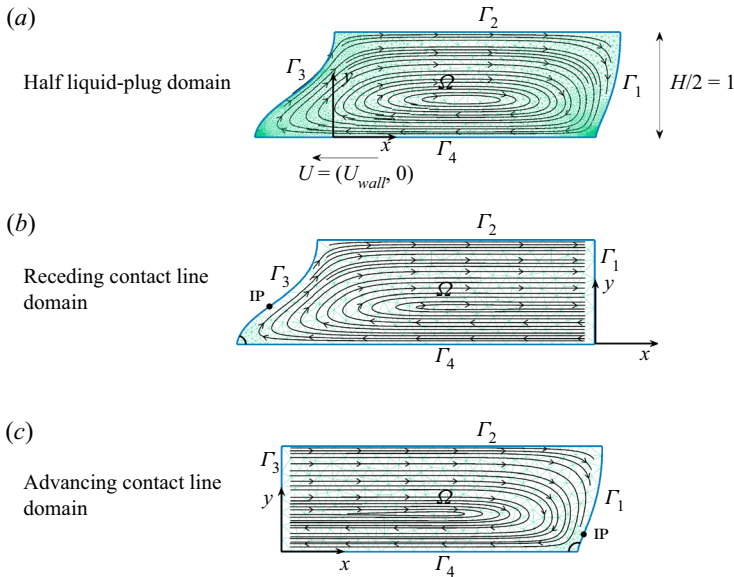domain

(*c*)

Advancing contact line
domain

Figure 3. The computational domain with streamlines and computational elements in the background. (*a*) Half-liquid plug domain – the upper boundary, Γ_2 is a symmetry boundary and Γ_4 is a moving wall, so we are computing the system in a frame of reference that moves with the liquid. (*b*) Receding contact line domain where, instead of a free surface at Γ_1, we impose parallel flow which significantly reduces the computational burden. (*c*) Advancing contact line domain. In (*b,c*) the circular markers on the free surfaces indicate the location of the inflection point, denoted IP. Parameter values are $Ca = Ca_{crit} = 0.31$, $\lambda = 0.1$, $\theta_{cl} = \pi/2$.

the arclength, s, as measured from the contact point. These are found using dynamic and kinematic conditions on both free surfaces. The governing equations and boundary conditions then become

$$0 = -\nabla p + \nabla^2 u + F, \quad x \in \Omega, \quad \text{Conservation of momentum}, \tag{2.1}$$

$$\nabla \cdot u = 0, \quad x \in \Omega, \quad \text{Incompressibility}, \tag{2.2}$$

$$\lambda(\tau \cdot n) \cdot t, = (u - U) \cdot t, \quad x \in \Gamma_4, \quad \text{Navier-slip condition}, \tag{2.3}$$

$$u \cdot n = 0, \quad x \in \Gamma_4, \quad \text{No-penetration condition}, \tag{2.4}$$

$$u \cdot n = 0, (\tau \cdot n) \cdot t = 0, \quad x \in \Gamma_2, \quad \text{Symmetry condition}, \tag{2.5}$$

$$\tau \cdot n = \frac{1}{Ca} \kappa n, \quad x \in \Gamma_1 \cup \Gamma_3, \quad \text{Dynamic condition (receding \& advancing)}, \tag{2.6}$$

$$\frac{\partial R_{adv}}{\partial t} \cdot n = u \cdot n, \quad x \in \Gamma_1, \quad \text{Kinematic condition (advancing)}, \tag{2.7}$$

$$\frac{\partial R_{rec}}{\partial t} \cdot n = u \cdot n, \quad x \in \Gamma_3, \quad \text{Kinematic condition (receding)}, \tag{2.8}$$

where n and t are the vectors normal and tangential, respectively, to the appropriate boundaries denoted Γ_i, and κ is the curvature of the corresponding interface. The plate speed $U = (U_{wall}, 0)^T$ and $\lambda = \lambda^*/(H^*/2)$ is the dimensionless slip length. The body force is $F = (F, 0)^T$, where F is a set constant. The stress tensor τ is defined as

$$\tau = -pI + \left(\nabla u + (\nabla u)^T \right), \tag{2.9}$$

953 A17-7

where I is the identity matrix. We shall refer to the system described by (2.1)–(2.8) as the 'half-liquid plug' problem.

2.2. *Contact angle models*

The system is not well-posed unless a contact angle is specified between the free surfaces and the horizontal plates. For the symmetry boundary, we set $\theta(s = L) = \pi/2$, but the dynamic contact angle, θ_{cl}, can be freely chosen and depends on the wettability of the solid.

The simplest approach is to specify a constant equilibrium contact angle, i.e.

$$\theta_{cl} = \text{const.,} \quad \text{Constant angle equation.} \tag{2.10}$$

However, as is well known, the MKT predicts θ_{cl} to be dependent on the speed of the contact line. As shown in Appendix A, for the RCLs of interest here, this dependence may be written in the linearised form

$$\overline{Ca} = \frac{\lambda}{\delta} \left(\cos(\theta_0) - \cos(\theta_{cl}) \right), \quad \text{VA equation,} \tag{2.11}$$

where δ is a dimensionless parameter that corresponds to the width of the TPZ, i.e. the contact line viewed at the molecular scale, and $\overline{Ca}$ is the relative velocity of the contact line to the wall speed, i.e.

$$\overline{Ca} = Ca \left(U \cdot e_x - \frac{\partial x}{\partial t} \bigg|_{s=0} \right), \tag{2.12}$$

where e_x is a unit vector in the x direction. Equation (2.11) is the linearised form of the theory, which will be valid for the system considered in this article. Furthermore, it has long been recognised that a relationship must exist between the slip length and the equilibrium contact angle, e.g. Tolstoi (1952), Barrat & Bocquet (1999) and Priezjev (2007). Here, motivated by the results of Fernández-Toledano *et al.* (2021) and the theory described in Appendix A, we consider the relationship

$$\lambda^*_{MD} = a \exp \left[b(1 + \cos(\theta_0)) \right], \quad 0 < \theta_0 < \pi, \tag{2.13}$$

where a and b are fitting parameters and λ^*_{MD} is the physical slip length derived from the MD data in Fernández-Toledano *et al.* (2021). We will assume that λ^*_{MD} is independent of the physical channel height, H^*, and, therefore, in our non-dimensionalisation $\lambda = 2\lambda^*_{MD}/H^*$. To investigate the nano-channel used in Fernández-Toledano *et al.* (2021), where $H^* = 20.2$ nm, the different values of θ_0 will yield dimensionless slip lengths in the range $\lambda \sim 0.02$ to 0.2. Alternatively, as we will show in § 7, by varying λ, and keeping θ_0 fixed, we can investigate the effects of varying the physical channel height H^* to larger systems. We emphasise that there is a one-to-one correspondence between λ^*_{MD} and θ_0, and hence, we are free to prescribe either quantity and use (2.13) to determine the other. In physical experiments it is more practical to find θ_0, which can readily be measured, and then determine λ^*_{MD}, which is more difficult to measure experimentally. Figure 4 shows the fit of this function to the MD data from Fernández-Toledano *et al.* (2021). We call the system of equations described in (2.1)–(2.8) augmented with the constant angle formula, (2.10), the constant angle (CA) model, while when augmented with the VA formula, (2.11) and (2.13), we call it the VA model.
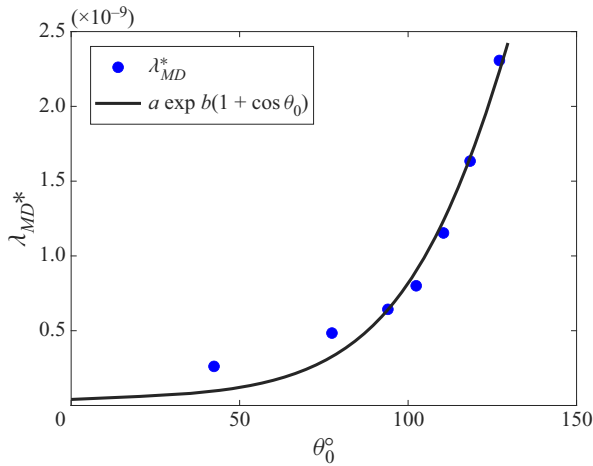
Figure 4. The slip length dependence on the static angle. The markers are the MD data obtained from Fernández-Toledano *et al.* (2021) and the solid line is the curve fit given from (2.13) with $b = -2.342$ and $a = 5.656 \times 10^{-9}$.

2.3. *Pressure-driven and force-driven problems*

We now discuss the two different types of problems, i.e. the pressure-driven and force-driven problems. The MD simulations in Fernández-Toledano *et al.* (2021) is a force-driven problem, but pressure-driven problems are relevant in many practical situations, for example, coating flows (Liu *et al.* 2019).

In Pouseille flow, without a free surface, it is easy to show that a pressure-driven problem can be equivalent to a force-driven one. With a free surface however, this is not true and each case has to be considered separately. For steady calculations, in both types of problems, the set of equations are ill-posed unless we specify the volume of the liquid plug. To remove this issue, for pressure-driven flow, we impose a normal stress on Γ_1,

$$\boldsymbol{\tau} \cdot \boldsymbol{n} = p_{out}\boldsymbol{n}, \quad \boldsymbol{x} \in \Gamma_1, \tag{2.14}$$

and let the value of p_{out} be determined implicitly by a condition on the overall volume of the liquid plug, which corresponds to the computational area of the domain. We set $F = 0$ and solve in a frame of reference that moves such that the walls are non-stationary in the translating frame ($U_{wall} = -1$).

In contrast, for the steady force-driven problem, we set $U_{wall} = -1$ and $p_{out} = 0$, but now let Ca be determined implicitly by a volume constraint. In both cases, to overcome the translational invariance, we also have to pin a point on the boundary that depends on the domain of the problem (as discussed below).

For time-dependent problems, whether pressure driven or force driven, the volume constraint is unnecessary, as (2.2) ensures that volume is conserved. Instead, we impose a position constraint for the reduced domains (see below) that determines p_{out} or Ca, depending on the problem.

2.4. *Numerical method*

The complete system of equations are discretised and solved using a finite-element method and the open-source oomph-lib package (Heil & Hazel 2006), as described in Keeler *et al.* (2021). An unstructured triangular mesh is used that is treated as a pseudo-elastic body,

so that changes to the unknown free surface can be facilitated and the mesh can adapt to capture regions of high velocity or pressure gradients, for example, near the contact point. We use a Zienkiewicz–Zhu (ZZ) error estimator, which measures the continuity of the rate of strain in each element, to identify elements that require refinement or unrefinement (Zienkiewicz & Zhu 1992). As a typical example, for the time-dependent calculations, with $Ca = 0.5$ and $\lambda = 0.01$, elemental areas range from $\sim 10^{-3}$ to 10^{-1} to accommodate a maximum ZZ error of 10^{-3}.

2.5. *'Half' and 'quarter' domains*

We can simplify the complexity of the half-liquid plug domain further by solving in two separate 'quarter' domains, each having only one free surface; thus, significantly reducing the number of triangular elements required, see figures 3(*b*) and 3(*c*). To facilitate this, we replace the free surface (and corresponding dynamic and kinematic boundary conditions) at one end of the computational domain (Γ_1 for the ACL and Γ_3 for the RCL) with an imposed normal stress (i.e. (2.14)) and parallel-flow condition

$$v = 0, \quad \boldsymbol{x} \in \Gamma_1 \text{ (Receding)} \quad \text{or} \quad \boldsymbol{x} \in \Gamma_3 \text{ (Advancing)}. \tag{2.15}$$

In these quarter domains, the imposed pressure, p_{out}, is determined implicitly by ensuring the volume per unit length (i.e. the area) of the liquid domain is constant (as in the half-liquid plug domain), so that in each quarter domain we are solving in a frame of reference with a fixed volume. We note that in the quarter domains we impose (2.14) and (2.15) in both steady and time-dependent calculations. These quarter domain simulations will be referred to as the 'receding contact line' and 'advancing contact line' domains (see figure 3*b*,*c*), respectively. abbreviated to RCL and ACL in the rest of the paper. The origin is different in each of these domains and corresponds to the pinned position of the steady and time-dependent problems. To illustrate the benefit of this reduction, the number of elements required in the computation of figure 5 for the half-liquid plug is $\sim$4000–8000, but the number for the RCL is $\sim$400. The reason for the $\sim$90 % reduction in elements is because the pressure gradients are not as severe near the RCL, compared with the ACL. In the next section we shall show that the dynamics of the whole system and the prediction of a critical Ca are dominated by the RCL. Thus, computation of the full half-liquid plug problem, where both the advancing and receding interface are calculated, is not necessary in order to find the first flow bifurcation and is computationally inefficient when compared with the reduced RCL domain.

We emphasise that the main aim of this study is to investigate the VA model, and not to make a thorough investigation of the differences between pressure-driven and force-driven flow, as the VA model can be applied independently of the problem. Thus, in the results that follow, we mainly consider pressure-driven flow, except when we make a direct comparison with the MD simulations. For the latter, we present force-driven results, as clearly specified. In addition, as we shall show in § 4.1, the choice of domain is also independent of the problem (i.e. pressure driven or force driven), so we choose the domain that is most important to the flow bifurcation and that is also the simplest, computationally.

3. Reduced governing equations (QP system)

We shall now discuss a reduced evolution partial differential equation model, the so-called QP system, before finally obtaining asymptotic results that will help predict the value of Ca_{crit}.
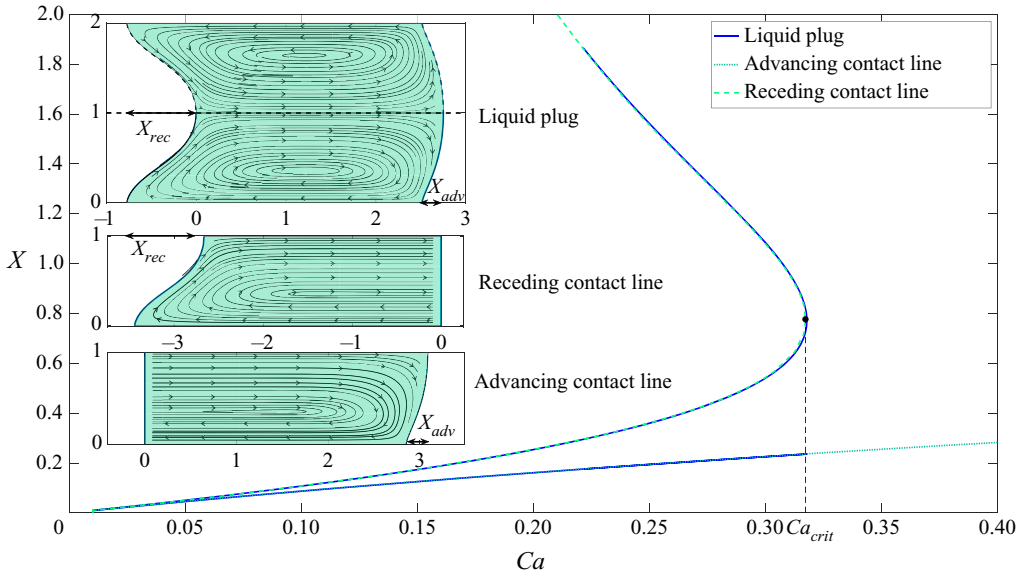
953 A17-10

Figure 5. The steady solution space mapped in the (Ca, X) plane when $\theta_{cl} = \text{const.} = \pi/2$. Here X_{adv} and X_{rec} are the horizontal distances of the interface at the two plates for the advancing and receding cases, respectively. The solid curves represent the half-liquid bridge problem, while the broken lines indicate the 'quarter' problems where the advancing and RCL are calculated separately. The limit point for the RCL indicates the threshold beyond which no steady states exist, denoted by Ca_{crit}, and corresponds to the critical F_0^* in the MD simulations of Fernández-Toledano *et al.* (2021). The inset diagrams correspond to the parameter values $Ca = Ca_{crit} \approx 0.31$, $\lambda = 0.2$.

For the RCL, the flow near the contact line is approximately parallel, cf. figure 12, and we can exploit this to reduce the Navier–Stokes equations to a simpler system that requires unknowns only on the fluid interface. As well as the parallel-flow assumption, we assume the horizontal coordinate is approximately the arclength, i.e. $x \approx s$, so the full expression for the curvature can be used, not the linearized form as used in conventional lubrication models (see, e.g. Eggers 2005) and long-wave models (see, e.g. Snoeijer 2006).

Following Jacqmin (2004), Sbragaglia, Sugiyama & Biferale (2008) and Vandre (2013), we let θ be the angle the interface makes to the horizontal (see figure 1), $h = y_r(s)$ be the height of the interface and s be the arclength coordinate measured from the contact line. Using conservation of mass and the kinematic condition on the free surface, the governing equation for the fluid pressure gradient, $\partial p / \partial s$, may be written as (Snoeijer *et al.* 2006)

$$\frac{\partial h}{\partial t} + \frac{\partial Q}{\partial s} = 0, \quad Q = \frac{\partial}{\partial s}\left(-\frac{1}{3}\frac{\partial p}{\partial s}h^2(h + 3\lambda) - (U \cdot e_x)h\right), \tag{3.1a,b}$$

where $U \cdot e_x = -1$ for the RCL. The unknown pressure gradient, $\partial p / \partial s$, can then be expressed in terms of the exact curvature by differentiating the normal stress balance with respect to s, i.e.

$$\frac{1}{Ca}\frac{\partial^2\theta}{\partial s^2} = \frac{\partial p}{\partial s}. \tag{3.2}$$

In order to solve (3.2), we require two conditions on θ. At the contact line, $s = 0$, we implement (2.11)

$$\overline{Ca} = \frac{\lambda}{\delta}\left(\cos(\theta_0) - \cos(\theta_{cl})\right), \tag{3.3}$$

953 A17-11

and at the symmetry wall, $s = L$, we set $\theta = \pi/2$, where L is the overall length of the interface. The shape of the interface can then be recovered by solving

$$\frac{\partial x}{\partial s} = \cos(\theta), \quad \frac{\partial h}{\partial s} = \sin(\theta). \quad (3.4a,b)$$

Each of these equations requires a single condition, so we set $x(s = 0) = y(s = 0) = 0$ (choosing the contact line to be at the origin). Finally, we note that the length of the interface, L, and, hence, the size of the domain, s, are not known *a priori*. To determine L, we scale the independent variable s, so that $\xi = Ls$ and $\xi = [0, 1]$. The total length of the interface, L, can then be determined by the additional constraint that

$$y(\xi = 1) = 1. \quad (3.5)$$

To solve this system of equations, we choose to discretise the spatial derivatives using finite differences and then the system of equations are solved numerically using Newton's method. We remark that we exclusively concentrate on the steady results of the pressure-driven QP system and do not solve the time-dependent problem, as this is better suited to the full nonlinear system.

3.1. *Asymptotics*

We now briefly describe and adapt the analysis of Chan, Snoeijer & Eggers (2012) and Eggers (2005) to find an asymptotic expression for Ca_{crit}. We will not repeat their analysis except for the parts where it differs from the situation we examine here. In both of these previous works gravitational effects are included and the liquid domain is unconfined, whereas we neglect gravity and the system is confined. They also considered only steady solutions, so that time derivatives in the problem can be ignored.

The matched asymptotics methodology of Chan *et al.* (2012) and Eggers (2005) is to determine an inner solution, say $h = h_{inner}$, for small Ca, that is valid close to the contact line, i.e. when $s/\lambda \sim O(1)$, and an outer solution, $h = h_{outer}$ say, that is valid far away from the contact line, i.e. when $s \sim O(1)$. To determine an unknown constant in the outer solution, the inner and outer solutions have to match in a crossover region. This matching procedure yields an equation, for an arbitrary unknown, θ_{app}, which is the angle the outer interface makes with the horizontal. For the ACL domain, θ_{app} is finite for all values of Ca, and thus, in these asymptotic limits at least, there is no critical point for the ACL domain. However, in the RCL domain θ_{app} can only be calculated up to a critical value of Ca, this value being interpreted as Ca_{crit}.

In our problem, for a confined geometry and in the absence of gravity, the inner region analysis near the contact line is identical to the case considered in Chan *et al.* (2012) and Eggers (2005). In Eggers (2005) the effects of gravity are present at first order in the outer solution. The outer solution, for small Ca, is found by expanding the unknowns as a power series in Ca. We can write a leading-order outer solution of (3.1*a,b*) to (3.4*a,b*) as

$$\left.\begin{array}{c} \theta_{outer} = \theta_{app} + \kappa_s s, \quad h_{outer} = 1 - \dfrac{1}{\kappa_s} \cos\left(\theta_{app} + \kappa_s s\right), \\[2mm] x_{outer} = \dfrac{1}{\kappa_s} \left[\sin\left(\theta_{app} + \kappa_s s\right) - 1\right] + X_{rec}, \end{array}\right\} \quad (3.6)$$

where $\kappa_s = (\pi - 2\theta_{app})/2L$ is the curvature, X_{rec} is the meniscus rise (cf. figure 5) and θ_{app} is an undetermined constant. The outer solution in (3.6) describes a sector of a circle with centre $(X_{rec} - r, 1)$ and $r = 1/\kappa_s$ that makes an angle θ_{app} to the horizontal at $s = 0$.
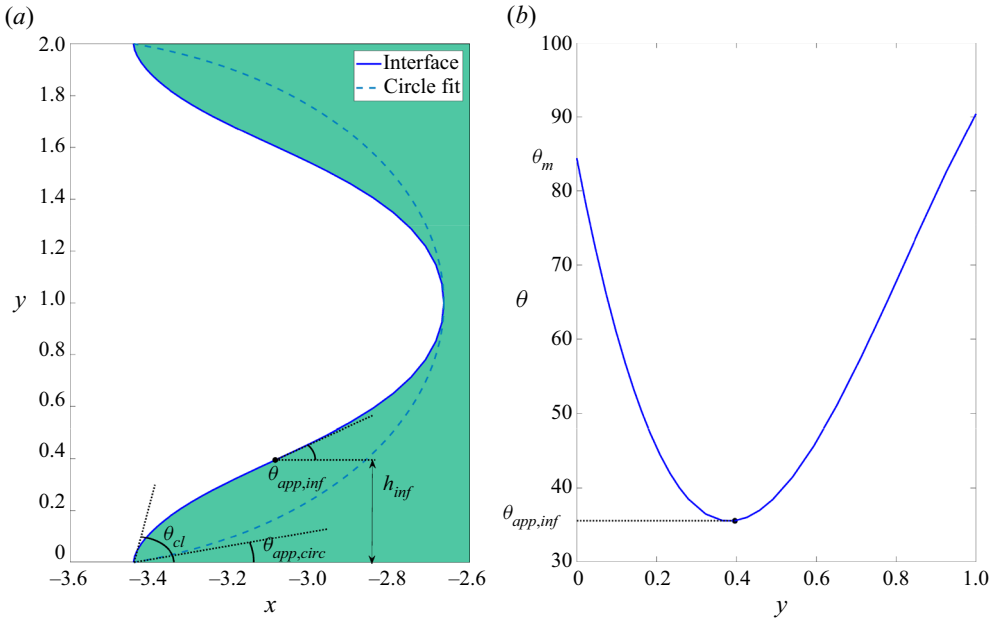
Figure 6. The alternative definitions of the apparent angle. In (*a*), $\theta_{app,circ}$ is defined as the angle a fitted circle makes with the bottom plate; $\theta_{app,inf}$ is defined as the minimum angle the interface makes with the horizontal, as measured anti-clockwise, and corresponds to the inflection point of the interface, where the curvature, $\kappa = 0$. In (*b*) we plot the interface angle as a function of y that demonstrates that $\theta_{app,inf}$ can be calculated as the minimum value of θ.

Examining the geometry (see dashed curve in figure 6*a*) gives $\kappa_s = \sin(\pi/2 - \theta_{app})$, so as $\theta_{app} \to 0$, $\kappa_s \to 1$ and, hence, the interface is a semi-circle of radius 1. In particular, we have

$$L \to \pi/2, \quad X_{rec} \to 1, \quad \text{as } \theta_{app} \to 0. \tag{3.7}$$

When the outer solution, described in (3.6), is matched to the inner solution, as described in Eggers (2005), we obtain an expression for θ_{app},

$$\frac{\theta_{app}}{\theta_{cl}^3} = -\frac{2^{2/3}3^{1/3}Ca^{1/3}\text{Ai}'(z_1)}{\text{Ai}(z_1)}, \tag{3.8}$$

where $\text{Ai}(z)$ is an Airy function of the first kind. We note this is the same for an unconfined geometry with gravity as considered in Eggers (2005). In addition, Ca_{crit} satisfies the same expression as in Eggers (2005) but has a factor of $2^{1/3}$ in the denominator of the logarithm term, i.e.

$$Ca_{crit} = \frac{\theta_{cl}^3}{9}\left[\log\left(\frac{Ca_{crit}^{1/3}\theta_{cl}}{3^{2/3} \cdot 2^{1/3}\text{Ai}^2(z_{max})\lambda\pi}\right)\right]^{-1}, \quad z_{max} = -1.0188. \tag{3.9a,b}$$

The difference between (3.9*a,b*) and the equivalent expression in Eggers (2005) is down to the far-field boundary conditions; in our problem the fluid is confined, and in Eggers (2005) it extends to infinity. These results are valid for a constant contact angle model but we can easily extend them to our VA formula by expanding (2.11) in powers of Ca, for $Ca \ll 1$, and then θ_{cl} in the above expression is just the static angle θ_0. However, we will show that the full expression for θ_{cl} in (2.11) will be required in the formula

953 A17-13

(3.9*a,b*) for it to compare favourably with the numerical results. In the sections that follow, the expressions in (3.7), (3.8) and (3.9*a,b*) will be compared with the numerical solutions.

4. System measurements and parameters

In this section we describe the methods used to determine Ca_{crit} from the numerical calculations of the fully nonlinear and QP systems. In addition we also discuss, in detail, the methodology of identifying the value of θ_{app}, and compare two different methods.

4.1. *Finding the critical Ca*

We now describe how we determine the critical *Ca* computationally. We note that this methodology is valid for both the fully nonlinear and QP systems. Initially, we shall assume a constant θ_{cl}, i.e. we impose (2.10), and, for simplicity, we shall assume that $\theta_{cl} = \pi/2$. In the pressure-driven problem, by varying *Ca* and subsequently solving the steady set of equations, we can trace the state of the system by recording the horizontal distance between where the interface meets the moving wall and the symmetry wall, which we denote X_{rec} and X_{adv} for the RCL and ACL, respectively (the same can be achieved in the force-driven problem by increasing the value of *F* and finding the maximum value of Ca_{crit}). Figure 5 shows the resulting solution curves of X_{rec} (upper curve) and X_{adv} (lower curve) plotted against *Ca*. The solid lines indicate solutions of the half-liquid plug problem, while the broken lines are solutions of the corresponding quarter RCL and ACL domains.

There are a number of important features of these solution curves. The RCL solution curve experiences a limit point (or fold bifurcation) where the curve turns around and the corresponding steady solution becomes unstable. The consequence of this is that the value of *Ca* where this critical point occurs marks the limiting threshold for which stable (i.e. those that can be experimentally realised) steady solutions exist, and it is, therefore, natural to associate this value with Ca_{crit}. It is important to emphasise that the limit point occurs only for the RCL in this set-up (i.e. a liquid–vacuum system). Furthermore, we note that the curves of the half-liquid plug problem completely overlap the curves for the RCL and ACL domains, the only distinction being that the quarter ACL solution curves are able to continue past Ca_{crit}, as no unstable ACL is observed. The critical point of the full nonlinear system coincides with the fold bifurcation of the RCL, and so in order to understand the dynamics of the system before and after criticality, we only need to consider the RCL; thus, significantly reducing the computational demands.

4.2. *Measuring the apparent angle*

The precision with which the dynamic contact angle can be measured experimentally is limited by the resolution of the method used (Dussan 1979). This is usually of the order of a few micrometres and, for optical measurements, can be no better than the diffraction limit. Thus, accurate measurement of the true contact angle is not possible, though some progress has been made (Chen, Yu & Wang 2014). A common approach is to fit a curve to the image of the interface and measure its tangent at its point of intersection with the solid surface. Alternatively, the interface can be assumed to have a quasi-equilibrium shape (e.g. a spherical cap) from which the angle may be deduced via an appropriate formula (Hoffman 1975; Dussan 1979; Chen, Ramé & Garoff 1995; Lhermerout & Davitt 2019). Neither approach has the ability to resolve significant changes in curvature very close to

the contact line, such as those observed in the MD simulations (see figure 2), which occur whenever the true contact angle differs significantly from the apparent angle. Therefore, to a greater or lesser extent, the measured angle inevitably depends on the method used to measure it, and simply represents the slope of the interface at some arbitrary distance from the contact line. This is the reason why these angles are commonly described as 'apparent'.

In the MD study, Fernández-Toledano *et al.* (2021), two methods were investigated to evaluate θ_{app} in a systematic way that was consistent with experiment, despite the very small scale of the system. For both, multiple snapshots were averaged to account for thermal noise. Since the menisci of the liquid plug are cylindrical at rest, the methods were based on circular fits to the liquid surface. The first approach was to estimate the slope of the interface at the point of its inflection, as shown in figure 6. This was achieved by fitting the arc of a circle to the central 50 % of the meniscus (i.e. well away from the inflections) and measuring the slope of the arc at its points of intersection with planes parallel to the solid surfaces and passing through the inflections. The method appealed as being consistent with the asymptotic matching procedure used in hydrodynamic treatments of dynamic wetting (Voinov 1976; Cox 1986).

The second approach was to mimic experiment more directly by measuring the tangents to a circular arc defined by upper and lower contact lines and passing through the apex of the meniscus at its mid-point, as shown in figure 6. This procedure is commonly used to measure the dynamic contact angle in capillary systems (Dussan 1979); and because the positions of the three defining points could be measured more accurately from the simulations than the locations of the inflections, this was the method adopted. It gave advancing angles a few degrees smaller than those found at the inflection points, but the receding angles were indistinguishable within simulation limits. The method was also used in a recent numerical study of microscopic and apparent contact angles (Omori & Kajishima 2017).

Similarly, in the present paper we calculate θ_{app} in two different ways consistent with those adopted in Fernández-Toledano *et al.* (2021). In figure 6(*a*) the liquid–gas interface is shown by a solid line and the arc of a circle that is tangent to the interface at the line of symmetry by a dashed line. We define $\theta_{app,circ}$ as the angle the circle makes with the horizontal as shown in figure 6. This definition, used in Fernández-Toledano *et al.* (2021), is useful if the position of the liquid–gas interface is not well defined.

Alternatively, and again as considered in Fernández-Toledano *et al.* (2021), we can define $\theta_{app,inf}$ as the angle the interface makes with the horizontal at the inflection point of the curve; see figure 6. In this definition we measure the angle along the curve using the identity

$$\theta \equiv \operatorname{atan}\left(\frac{y'(s)}{x'(s)}\right) \tag{4.1}$$

and then find the minimum value that θ takes as a function of *x*; see figure 6(*b*). This corresponds to where the curvature is zero and the interface has an inflection point. The value of *y* at the inflection point is denoted h_{inf}, which will be commented on later in the paper. This approach of measuring θ_{app} is more amenable to finite-element method calculations, because (4.1) can be calculated easily as the position of the interface is well defined and was the approach used in Liu *et al.* (2019), Vandre *et al.* (2012), Liu *et al.* (2016*a*,*b*,2017) and Vandre *et al.* (2013).

953 A17-15

5. Steady results

In this section we will describe the steady solution space of the RCL using and comparing the CA model, where θ_{cl} is held constant, and the VA model, where θ_{cl} is determined by (2.11). First, using parameter values that are representative of the values in Fernández-Toledano *et al.* (2021), we shall compute steady solutions in the pressure-driven VA model and present a bifurcation diagram that demonstrates that the fold bifurcation, which represents the critical speed of dewetting, still exists when using the VA model and predicts the value obtained in Fernández-Toledano *et al.* (2021). Then we shall vary θ_0 to investigate the effect of wettability on the value of Ca_{crit} and compare this directly with the results of Fernández-Toledano *et al.* (2021) using the pressure-driven and force-driven problem. Finally, we compare the predictions of the continuum model with the results previously obtained by applying the Cox–Voinov law to the data derived from the MD simulations in Fernández-Toledano *et al.* (2021).

5.1. *Bifurcation diagram and general features*

We now focus our attention to the VA model and discuss steady solutions and the critical point. We emphasise that in this model we require only the static angle, θ_0, the width of the TPZ, δ, and the capillary number, Ca, as specified parameters so that a steady solution can be computed.

Figure 7 shows the steady solution space of the RCL domain by plotting X against Ca, as calculated numerically. The solid and dashed curves indicate, respectively, the stable and unstable solution branches of the full system and the circular markers indicate the solution branch of the QP system. The inset diagrams show streamline patterns and the interface position at (A) the critical point, (B) when $\theta_{app,circ} = 0$ and (C) when $\theta_{app,inf} = 0$. There are a number of interesting features that are worth commenting on. First, we note that even though θ_{cl} is now dependent on Ca, the limit point still occurs. We also remark on the close agreement of the QP system and the full nonlinear system; the QP system does remarkably well in approximating the limit point for this particular value of θ_0, although the curves diverge as X_{rec} increases.

The solution where $\theta_{app,circ} = 0$ is significantly closer on the bifurcation curve to the limit point than where $\theta_{app,inf} = 0$. In fact, as seen from the inset interface profiles, the interface when $\theta_{app,inf} = 0$ (label (C)) is already significantly deformed and approaching a thin film, whereas the profile when $\theta_{app,circ} = 0$ (label (B)) more closely matches the interface at the limit point (label (A)). This result is interesting, as in many works, e.g. Eggers (2005), Ca_{crit} is defined as occurring when $\theta_{app} = 0$. This is strictly valid in the regime $\lambda \to 0$ and we note that in our geometry the slip length and Ca take moderate values, and therefore, we find that $\theta_{app} \neq 0$ at Ca_{crit}.

The consequence of our findings is that it is not unreasonable to use the definition of $\theta_{app,circ} = 0$ as a lower bound on the critical capillary number when analysing outcomes in experiments and MD simulations where the existence of a smooth bifurcation curve is hidden, including smaller geometries whose dimensions are comparable to those of the slip length. Furthermore, at the limit point, we expect the dynamics of the system to be very slow, as the leading eigenvalue of the linear stability problem will be close to zero (Keeler *et al.* 2021). Thus, in any experimental/MD set-up the time frame may not be large enough to guarantee that a steady state is being approached or whether a thin film is about to develop. Therefore, we conclude that while the position of the critical point is a well-defined threshold for the critical capillary number in calculations involving a deterministic hydrodynamic model, for experimental and MD results, using the definition of Ca_{crit} as the location where $\theta_{app,circ} = 0$ may be operationally acceptable.
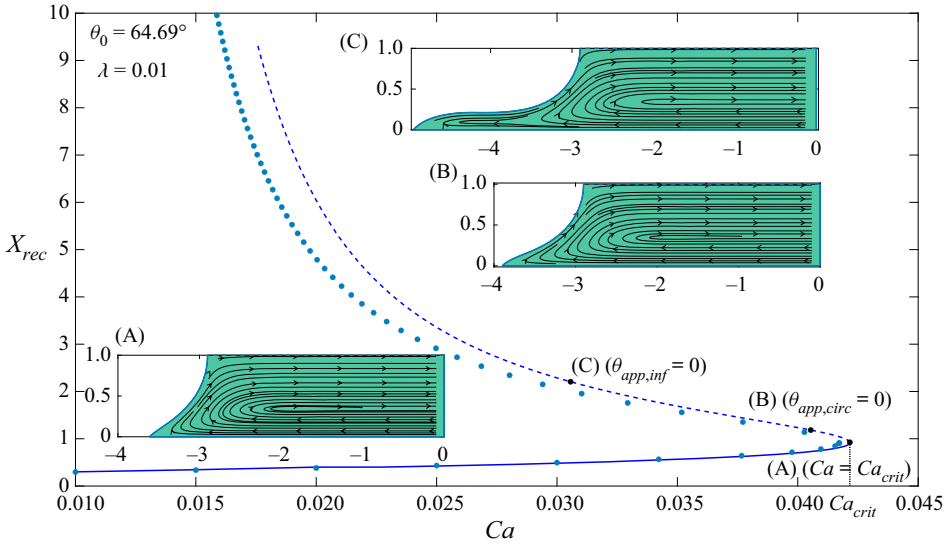
Figure 7. The steady solution structure for $\theta_0 = 64.7°$ and $\lambda = 0.02$. The solid/dashed curves indicate the stable/unstable branches of the full VA system and the solid circular markers indicate the solution using the QP approach. The inset profiles show the steady solution interface and domain when (A) $Ca = Ca_{crit}$, (B) $\theta_{app,circ} = 0$ and (C) $\theta_{app,inf} = 0$. Their locations are indicated by solid black markers on the main curve.

The difference between $\theta_{app,circ}$ and $\theta_{app,inf}$ for both the RCL and ACL is shown in figure 8 for values of $\lambda = 0.2$ and $\theta_0 = 105°$. As Ca_{crit} is approached in the RCL domain, the apparent angle tends to zero in a way such that $\theta_{app,circ} < \theta_{app,inf} < \theta_{cl}$. For the ACL domain (the shaded region in the figure), the order of the inequalities is reversed, although there is less of a distinction between $\theta_{app,circ}$ and $\theta_{app,inf}$. We should also mention here that in the original MD study (Fernández-Toledano *et al.* 2021) the behaviour of the cosine of the advancing contact angle was significantly nonlinear over the range of velocities investigated. As a result, the difference between θ_{cl} and $\theta_{app,circ}$ was significantly smaller than that depicted in figure 8, where the linear form of the MKT, (2.11), is used throughout.

5.2. *Behaviour of Ca_{crit}: VA and CA model versus MD*

A critical test of both the CA and VA model is how well it is able to predict Ca_{crit} when compared with the MD. For the CA model, we specify λ and θ_{cl} and then Ca_{crit} can be calculated using the method described in Keeler *et al.* (2021) to find the fold bifurcation. Figure 9(*a*) shows the location of Ca_{crit} as θ_{cl} is varied for $\lambda = 0.02$ and $\lambda = 0.2$; these values roughly corresponding to the lower and upper bounds of the slip length in the MD calculations. As can be seen from the figure, the comparison with the MD data is poor, with Ca_{crit} underestimated. This provides motivation to implement a VA model where θ_{cl} is a function of Ca and λ.

A much more convincing result is obtained when we apply the VA model. Figure 9(*b*) shows Ca_{crit} plotted against θ_{cl}. The curves represent the loci of the critical point as λ and, therefore, θ_0, are varied. Note that λ and θ_0 are expressly linked by expression (2.13). Here, we have chosen a range of λ that matches the MD simulations in Fernández-Toledano *et al.* (2021); the only parameter we have to specify is δ in (2.11). The solid/dotted lines are for the pressure-driven/force-driven problems, respectively, with $\delta = 0.0525$, the value from
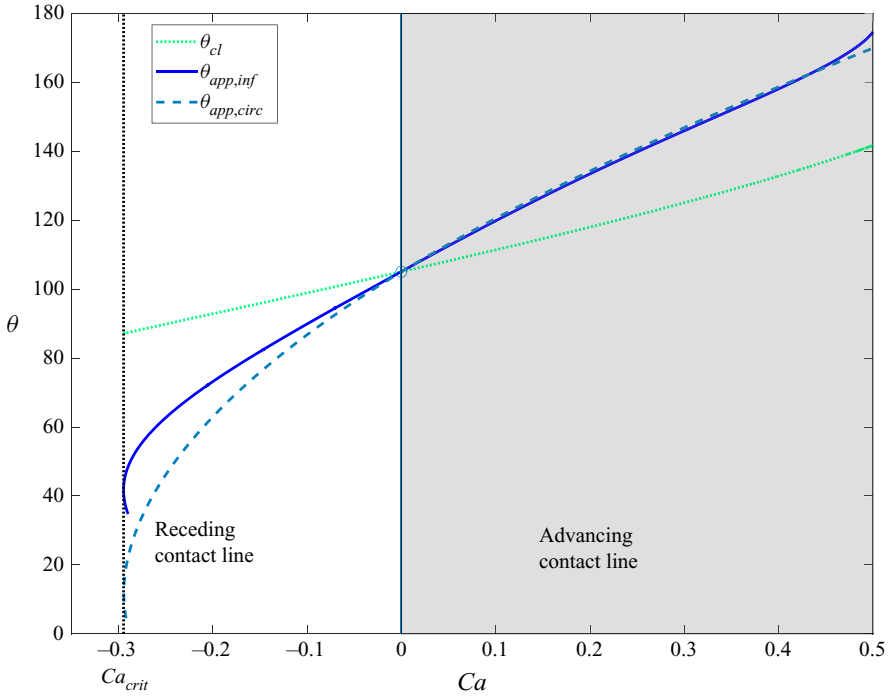
Figure 8. (*a*) The measured angles as a function of *Ca* when $\lambda = 0.2$, $\theta_0 = 105.1°$. In this figure we adopt the convention of Fernández-Toledano *et al.* (2021) where, for the RCL domain, *Ca* is negative.
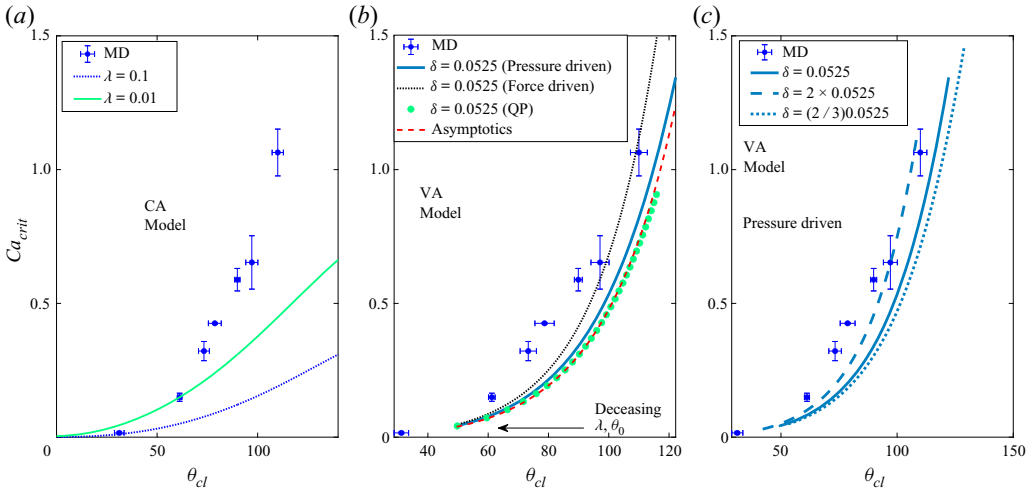

Figure 9. In each chart, the markers with error bars are the MD data obtained from Fernández-Toledano *et al.* (2021). (*a*) The critical *Ca* as a function of the true angle, θ_{cl}, for different values of λ using the constant θ_{cl} model given in (2.10). (*b*) The critical *Ca* as a function of the true angle, θ_{cl}, for the pressure-driven (solid line) and force-driven (dotted line) problems, QP system (circular markers) and the asymptotics given by (3.9*a,b*) (dashed line). (*c*) The critical *Ca* as a function of the true angle, θ_{cl}, for different values of δ. The value of $\delta = 0.0525$ corresponds to that obtained from the simulations in Fernández-Toledano *et al.* (2021).

953 A17-18

the MD simulations; see Appendix A. The solid markers are the QP data and the dashed line is the asymptotics described by (3.9*a,b*).

Remarkably, the QP model replicates the full nonlinear system and the simple asymptotic formula shows excellent agreement with the QP model, despite this being in a regime when the slip length, and indeed *Ca*, are not particularly small. We stress that here the asymptotic formula uses the full *Ca*-dependent formula for θ_{cl}.

Evidently, the VA theory captures the same qualitative behaviour exhibited by the MD simulations and is much better at predicting Ca_{crit} than the CA model and the force-driven problem has a slightly better quantitative fit. For the value of δ obtained from Fernández-Toledano *et al.* (2021), the VA under predicts Ca_{crit} for the same value of θ_0, but if we make δ larger the comparison becomes more favourable, as shown by the dashed line in figure 9(*c*). The uncertainty in selecting the appropriate basis for the measurement of δ from the simulations is discussed in Appendix A. Values of δ larger than that used here are certainly compatible with the data, depending on the criteria used to define the TPZ. This uncertainty is compounded by the inevitable thermal noise in the MD results, despite averaging the data over long periods relative to the simulation time scale, which means that there is an inherent difficulty in obtaining the exact steady state at the critical point in the MD simulations. This would mean that the critical point from the MD simulations should be treated as a lower bound, rather than a precise value.

As well as measuring θ_{cl}, we also measure $\theta_{app,inf}$ and $\theta_{app,circ}$ at the limit point. Figure 10 shows three curves that represent the Ca_{crit} as a function of (1) $\theta_{app,circ}$, (2) $\theta_{app,inf}$ and (3) θ_{cl}. We observe that $\theta_{app,circ}$ at Ca_{crit} never exceeds $20°$, which is consistent with experimental studies of the apparent angles at RCLs (de Gennes 1986; Redon, Brochard-Wyart & Ronelez 1991; Brochard-Wyart & de Gennes 1992; Rio *et al.* 2005), where the data shows that $\mathrm{d}\theta_{app}/\mathrm{d}Ca$ diverges rapidly as $Ca \to Ca_{crit}$, and is replicated in the VA model as shown in figure 8. In these previous studies apparent angles approaching zero are reported only on surfaces that exhibit little or no contact angle hysteresis (Lhermerout & Davitt 2019). Hysteresis implies the presence of surface imperfections, such as roughness or heterogeneity. These cause local fluctuations in contact line velocity, which may trigger film deposition prematurely. This might be the reason why Rio *et al.* (2005) report that angles below about $30°$ were inaccessible. The alternative possibility is that dewetting systems may become intrinsically unstable at some value of $\theta_{app} > 0$, as demonstrated here. The fact that θ_{app} is itself an artificial construct and dependent on the method of observation adds further uncertainty to the interpretation of experimental data. Nevertheless, we comment that the results from the VA model are consistent with these experimental observations.

We shall now use the Cox–Voinov law, (1.1), to help further rationalise the MD results. If we interpret θ_{app} as $\theta_{app,circ}$, the approach taken by Fernández-Toledano *et al.* (2021), we can make the approximation that $\theta_{app,circ} = 0$ at the critical capillary number and then (1.1) reduces to

$$\theta_{cl}^3 = 9\,Ca_{crit} \log\left(L^*/L_m^*\right). \tag{5.1}$$

We replicate the method of Fernández-Toledano *et al.* (2021) to obtain an 'estimate' of L^*/L_m^*, using (5.1). We do not expect L^*/L_m^* to be constant, given (2.13), but the purpose of this calculation is to perform a quantitative comparison with the MD data in Fernández-Toledano *et al.* (2021), rather than a comparison with the asymptotic theory of Cox, which is not wholly appropriate in our geometry as the slip lengths are not asymptotically small. In figure 11 we plot θ_{cl}^3 as a function of Ca_{crit}, based on the solutions at Ca_{crit} for each value of θ_0. We can 'estimate' the value of L^*/L_m^* by approximating the curve as a straight line and measuring the slope. The figure demonstrates that a straight
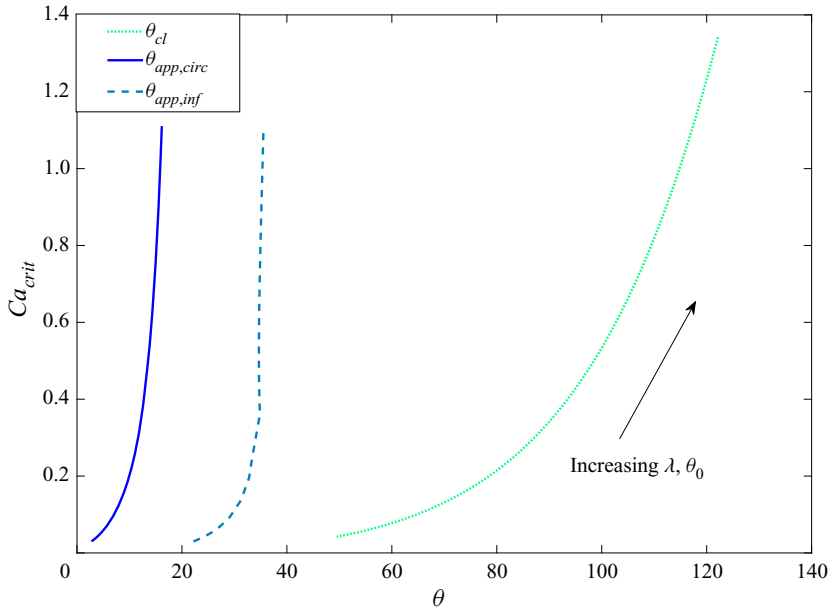
Figure 10. The critical Ca as a function of the true angle for $\delta = 0.0525$ with the values of $\theta_{app,circ}$ and $\theta_{app,Inf}$ also shown. Note that $\theta_{app,circ}$ only approaches zero as $\lambda \to 0$.
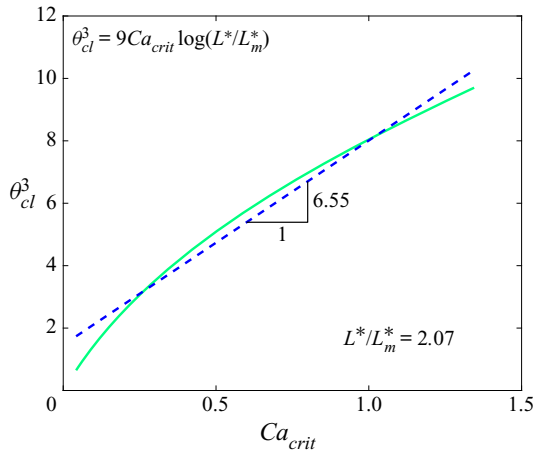

Figure 11. Exploiting the Cox–Voinov law. The solid curve is θ_{cl}^3 against Ca_{crit} as calculated using the full nonlinear model. The dashed line is a line of best fit with the gradient corresponding to $L^*/L_m^* = 2.07$.

line is not wholly appropriate, but its slope gives an approximation of $L^*/L_m^* = 2.07$, which compares favourably with the equivalent approximation from Fernández-Toledano *et al.* (2021) of 2.06 (denoted L/L_m in their study). This is further direct evidence that the numerical results of the model closely replicate the MD simulations.

6. Time-dependent results: thin-film formation

We now discuss time-dependent calculations and the formation/deposition of a thin liquid film. In most of the simulations that follow, we start a pressure-driven system from rest
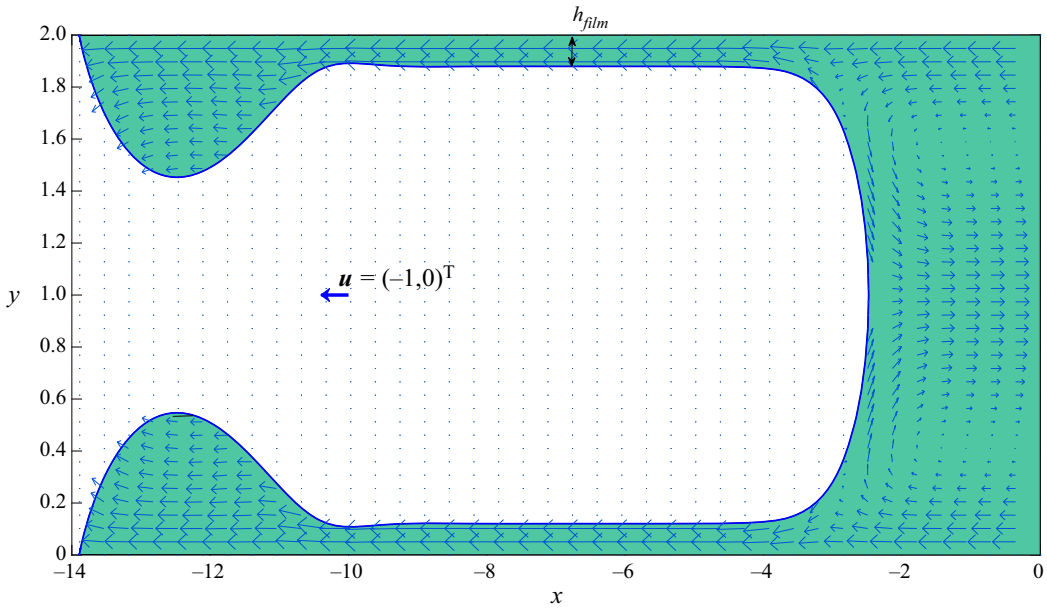
953 A17-20

Figure 12. Quiver plot of the thin film. Here $Ca = 0.05$, $\lambda = 0.02$, $\theta_0 = 64.7°$, $t = 19.9$. The arrows indicate the relative size of the local velocity vector field. The blue arrow indicates the scale of a unit vector.

with an initially flat interface and a constant value of Ca. As shown in Keeler *et al.* (2021), if we choose $Ca < Ca_{crit}$ then the system will relax to the stable steady solution branch, as seen in the MD simulations when $F_0^* < F_{crit}^*$. However, if we choose $Ca > Ca_{crit}$, a thin film will develop, as also observed in the simulations. In this section we implement (2.11) and perform time-dependent calculations to understand the effect of the various parameters on the formation of this thin film.

Figure 12 is a visualisation of the velocity field using quivers to represent the strength and direction of the flow once a thin film has developed. There are three distinct regions; a 'rim' region close to the contact line, a flat, thin-film region of height h_{film} and a static region corresponding to the static meniscus shape. We remark that close to the contact line the flow is approximately parallel, and so a lubrication model would be an appropriate model reduction here. Far away from the contact line, the flow is certainly not parallel and, therefore, to resolve the half-liquid plug a full continuum model is required.

Figure 13 shows snapshots of the evolution of the interface at different times, t, for various values of Ca (panels *a–d*). Panel (*e*) shows the time signal of θ_{cl} and panel (*f*) compares the final time snapshot for the different values of Ca chosen. In the supercritical case (i.e. $Ca > Ca_{crit}$) the height of the thin film is approximately constant before an almost circular cap region closes the interface. For macroscopic geometries, it is well known that the film thickness, h_{film} scales according to the Landau–Levich–Derjaguin law (Deryaguin 1943; Landau & Levich 1988)

$$h_{film} \sim 0.95 Ca^{2/3}, \quad Ca \ll 1. \tag{6.1}$$

This value of the film height is shown as dotted lines in figure 13(*b–d*) and the actual thin films closely match this value with increasing accuracy as Ca becomes smaller (as expected).
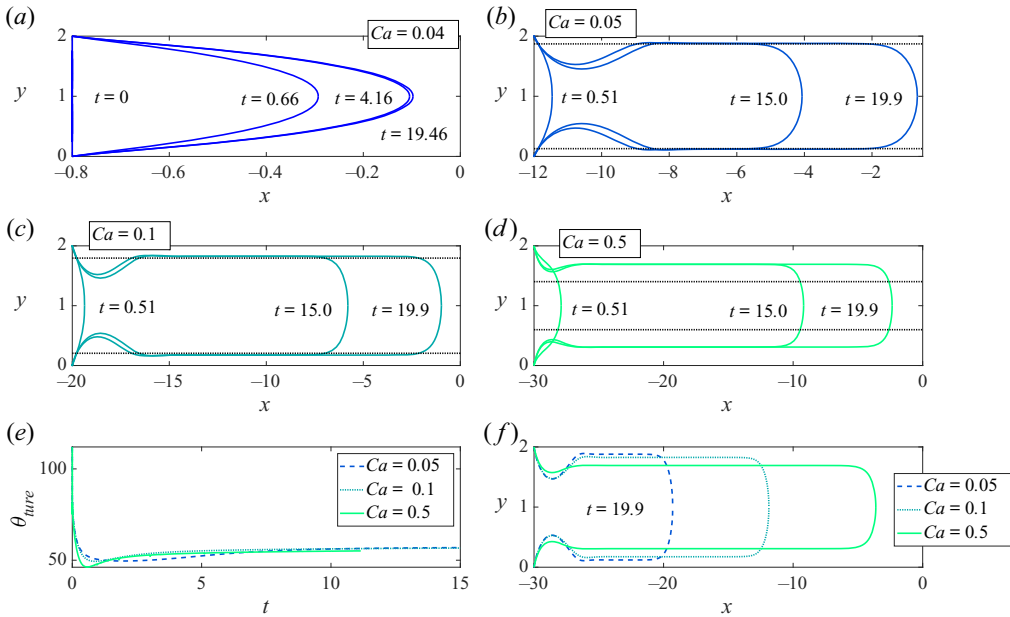
Figure 13. Time-dependent calculation when $\theta_0 = 64.7°$ (or $\lambda = 0.02$). (*a*) In this panel, $Ca = 0.04 < Ca_{crit}$. The system settles on the stable steady state and a thin film is not formed. Plots (*b–d*) show the thin-film formation for $Ca = 0.05, 0.1, 0.5 > Ca_{crit}$, respectively. The dotted lines indicate the Landau–Levich–Derjaguin film height, given in (6.1). Plot (*e*) shows the evolution of θ_{cl} as a function of t. Plot (*f*) compares the thin-film profiles for different Ca when $t = 19.9$. Note the scale of the horizontal axes on (*a–d*) are different.

The contact angle at small times rapidly decreases and achieves a minimum value, before gradually increasing to a limiting value, at $\theta_{cl} \approx 59°$, as shown in panel (*e*); the same time-dependent behaviour was observed in the MD simulations. A key observation is that in these time-dependent calculations the limiting relative capillary number $\overline{Ca}$ is independent of Ca, as seen in figure 14(*a*), which is consistent with experimental and theoretical studies, for example, Snoeijer *et al.* (2006). This indicates that the flow in the film region becomes increasingly independent of the liquid plug. In Keeler *et al.* (2021) it was shown that, at the RCL especially, the time-dependent trajectories of the system are similar to the steady bifurcation diagram when both are plotted in the $(\overline{Ca}, X)$ plane. The same phenomenon occurs here; see panel (*b*) in figure 14 where it is shown that the trajectories closely match the steady bifurcation curve. This is consistent with a prediction of Chan *et al.* (2012) that, for plate withdrawal from a bath flattened in the far field by gravity, the dynamics closely follow the unstable branch of solutions in a quasi-steady manner. In their case, where gravity plays an important role, the bifurcation curve oscillates around a fixed value of Ca, but in the pressure-driven problem this does not occur and we observe monotonic convergence towards a particular Ca. In the body-force problem we see the exact same phenomena, for both the CA and VA model (results not shown), but leave a thorough investigation of this as a future research avenue. Finally, we can make a qualitative comparison of the numerical results to the MD results in figure 2. Figure 15 shows the equivalent half-liquid plug profiles for the force-driven problem (as in the MD) obtained by computing the receding and advancing interfaces separately and combining them. As can be seen from the profiles, the qualitative comparison is strong.
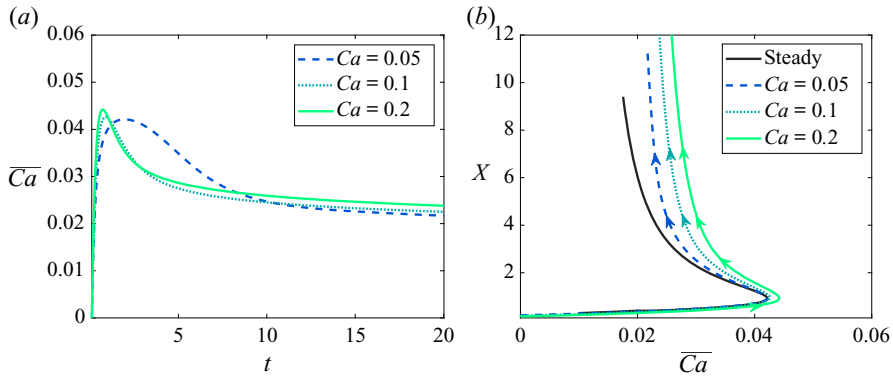
Figure 14. (*a*) Time signal of $\overline{Ca}$ defined in (2.12) when $\theta_0 = 64.7°$ (or $\lambda = 0.02$, for $Ca = 0.05, 0.1, 0.5 > Ca_{crit}$, respectively. (*b*) Comparison of time trajectories with the steady solution curve in the $(\overline{Ca}, X)$ plane.
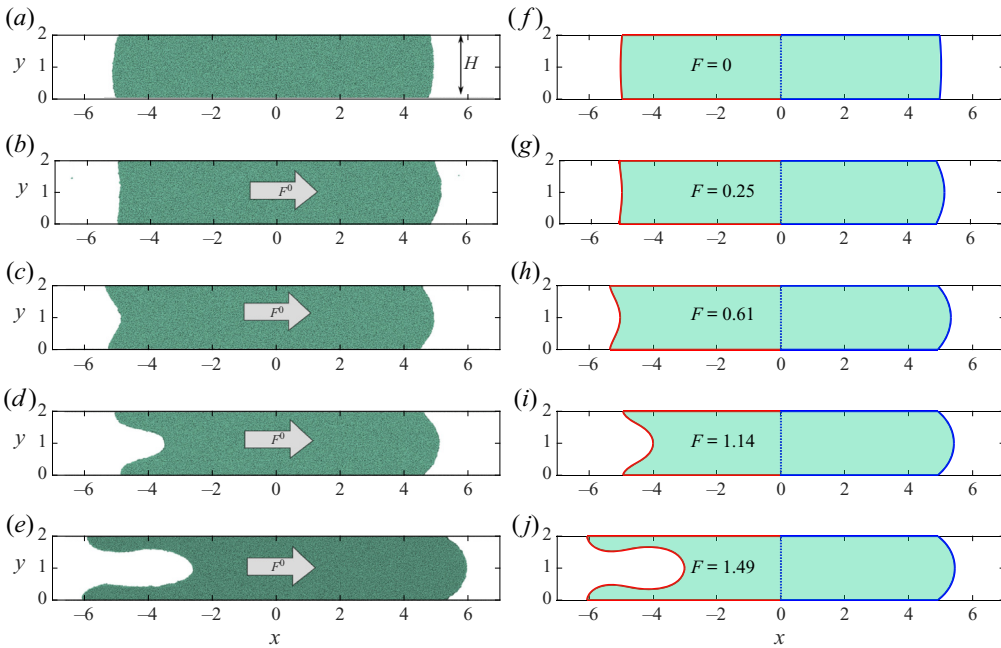

Figure 15. Qualitative comparison with figure 2 (figure reprinted from Fernández-Toledano *et al.* (2021), with permission from Elsevier) when $\theta_0 = 102.4°$. The left column are the images taken from figure 2 and the right column are calculations using the force-driven problem with the value of F stated.

7. Larger-scale systems

Having validated our model in the context of the nano-geometry using MD calculations, we can extend our analysis to investigate thin-film formation in a larger-scale geometry, for which MD simulations are prohibitively computationally expensive. We can achieve this by reducing the value of the dimensionless slip length λ while keeping θ_0 and, therefore, the physical slip length constant, which has the effect of increasing H^*, the physical channel width.
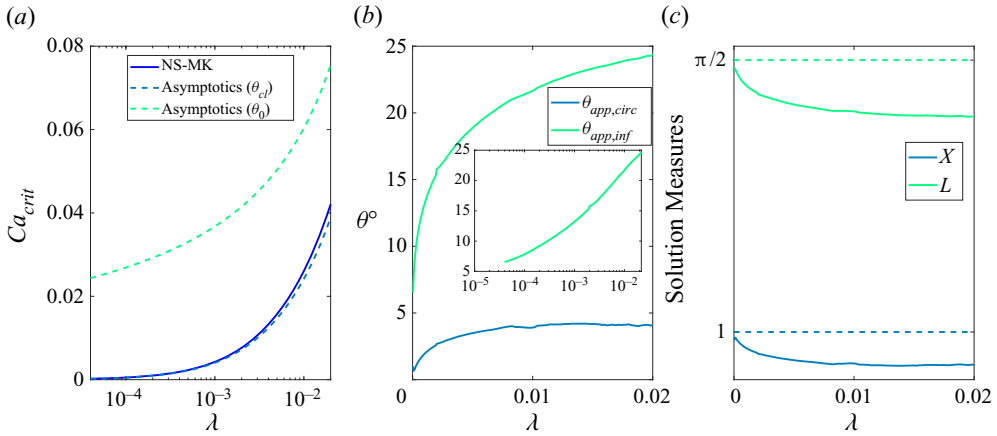
Figure 16. (*a*) The evolution of Ca_{crit} as λ is varied for $\theta_0 = 64.7°$. The numerics are indicated by the solid curve and the asymptotics given in (3.9*a,b*) are shown with a dashed curve when θ_{cl} is used in (3.9*a,b*) and a dotted curve when θ_0 is in (3.9*a,b*). (*b*) The variation of $\theta_{app,circ}$ and $\theta_{app,inf}$ at the critical point, shown as dashed and solid lines, respectively. The inset diagram is the same data shown on a log scale. (*c*) The variation of X and L at the critical point as λ is varied.

We also investigate the formation of thin films in the limit as $\lambda \to 0$ (we note that $\lambda = 0$ has no solution (Huh & Scriven 1971)). Using the same methods as before, we can track Ca_{crit} as λ is varied. Figure 16(*a*) shows that $Ca_{crit} \to 0$ as $\lambda \to 0$, indicating that the system becomes unstable for increasingly slower wall speeds as the scale of the system is increased. The dashed line indicates the asymptotic formula given in (3.9*a,b*), with the full expression for θ_{cl} used, and the dotted line shows (3.9*a,b*) with θ_{cl} replaced with θ_0. Because $\lambda \ll \delta$, the difference between θ_0 and θ_{cl} is large; see (2.11). As a result, in order to capture the numerics, the full expression for θ_{cl} has to be included in the asymptotic formula, and then the agreement is excellent.

Figure 16(*b*) shows how $\theta_{app,circ}$ and $\theta_{app,inf}$ vary at the critical point. It is clear that, for both measures of the apparent angle, as λ decreases, $\theta_{app} \to 0$. This is an important observation and provides a link to the work of Snoeijer *et al.* (2006, 2007), Eggers (2004), where in the lubrication approximation they apply, it is perfectly reasonable to employ the Cox–Voinov formula with $\theta_{app} = 0$ as a means of determining Ca_{crit}. In a nano-geometry however, this approximation is not valid, as we have shown that $\theta_{app,crit} \neq 0$. We also find that, as $\lambda \to 0$, the interface approaches a circular meniscus with radius 1 and length $\pi/2$, as the results in panel (*c*) clearly show.

We now turn our attention to time-dependent results in the limit as $\lambda \to 0$ with θ_0 being kept fixed. Figure 17 shows the thin film at $t = 14.916$ for values of $\lambda = 2 \times 10^{-2}, 2 \times 10^{-3}, 2 \times 10^{-4}, 2 \times 10^{-5}$ (panels *a–d*) with $Ca = 0.05$, $\theta_0 = 64.7°$. The largest value of $\lambda = 0.02$ corresponds to the nano-channel considered in Fernández-Toledano *et al.* (2021) while the smallest value of 2×10^{-5} corresponds to a system 10^3 times larger, i.e. a micro-channel. Figure 17(*e*) shows the comparison of the profiles when the x is normalised by X. The immediate observation is that the dimensionless film height, h_{film}, is independent of λ once the thin film has had sufficient time to develop, so that the physical film height will scale linearly with the system size. This is especially evident when comparing the interface profiles for $\lambda = 2 \times 10^{-3}, 2 \times 10^{-4}, 2 \times 10^{-5}$. Thus, sufficiently far away from the contact line the structure of the thin film is independent of the size of the geometry (in physical systems this is measured relative to the physical width of the channel).
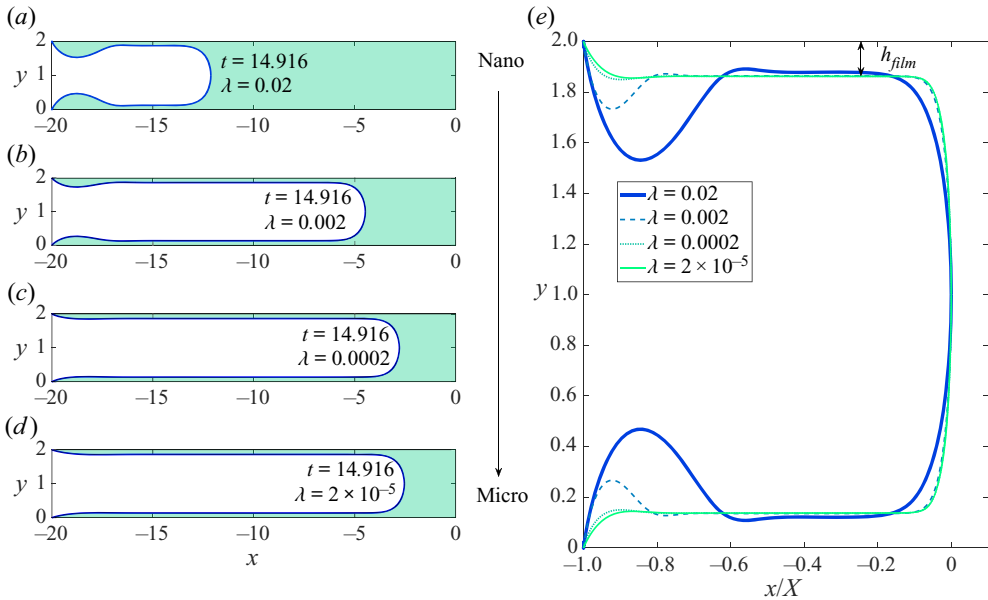
953 A17-24

Figure 17. Thin-film formation when the scale of the system is increased. Panels (*a–d*) show the thin film at $t = 14.916$ for $\lambda = 0.02, 0.002, 0.0002, 0.00002$ and $Ca = 0.05$, $\theta_0 = 64.7°$. Panel (*e*) shows a comparison of each of the profiles in (*a–d*) scaled by X.

The 'rim' region is however highly dependent on λ and the details of the contact line angle (see Flitton & King 2004); the smaller the system (larger λ) the larger the 'rim' near the contact line. Therefore, the physical rim height will increase slower than linearly as the system size is increased.

8. Conclusion

We have developed a novel molecularly augmented continuum model, based on a variable true contact angle, that describes the dynamics of a liquid bridge between two parallel plates, and, more generally, describes the RCL and ACL physics. By solving the resulting set of equations numerically, we are able to interpret the maximum speed of dewetting as a fold bifurcation in the steady bifurcation diagram. We find that the maximum speed of wetting Ca_{crit}, calculated as a function of θ_{cl}, is qualitatively similar to the MD simulations described in Fernández-Toledano *et al.* (2021) and that the estimate of L^*/L_m^* is in excellent agreement.

As well as showing good agreement with the MD simulation, the advantage of this approach is that by replacing the assumption that θ_{cl} is constant with the constraints

$$\left.\begin{array}{l}\overline{Ca} = \dfrac{\lambda}{\delta}\left(\cos(\theta_{cl}) - \cos(\theta_0)\right), \\[2mm] \lambda_{MD}^* = a\exp\left[b(1 + \cos(\theta_0)\right], \end{array}\right\} \tag{8.1}$$

the issue of deciding what θ_{cl} should be in any hydrodynamic calculation is removed, as it is naturally determined, through (8.1), as part of the solution. Furthermore, whereas in previous approaches the slip length and θ_{cl} had to be specified as control parameters, in this model the only hydrodynamic parameter we have to specify is the slip length. With this parameter being difficult to measure, invariably it has been used as an additional

fitting parameter that can cover up for inaccuracies in the constant angle model. We do however have to estimate δ, the width of the TPZ from MD simulations and this provides an additional parameter that has to be known in advance, although this parameter can be far more accurately specified than slip lengths. The comparison between the MD simulations and the VA model is strong, and although some of the physics present in the MD calculations are absent, for example, the disjoining pressure, we conclude that the VA model contains the minimum ingredients required to replicate the physics contained in the MD calculations, at least before the thin film ruptures (see, e.g. Kreutzer *et al.* 2018; Zhao *et al.* 2018).

Our results also illuminate the values of θ_{cl} and θ_{app} when a partially wetted substrate is withdrawn from a pool of liquid at capillary numbers greater than Ca_{crit}. Experiments have shown that attempts at forced dewetting cause the (three-dimensional) contact line to slant at an angle relative to the direction of withdrawal, such that the capillary number in the direction normal to the contact line remains constant at Ca_{crit}. These observations of avoided critical behaviour led to the postulate of a maximum speed of dewetting (Blake & Ruschak 1979). Presumably, θ_{cl} and θ_{app} along the slanted contact line are the smallest possible consistent with a stable flow without film deposition, i.e. those associated with the turning point in the steady phase diagram. For θ_{cl}, this is $\theta_{cl,crit}$. For θ_{app}, it depends on how the angle is measured.

We are easily able to extend the VA model to larger systems, which are prohibitively computationally expensive for MD calculations, and by examining the thin-film formation in these systems when $Ca > Ca_{crit}$, we are able to demonstrate that the relative height of the thin film is independent of size of the system and weakly dependent on Ca. Differences in the interface profile occur close to the contact line, as indicated by the size of the 'rim' that develops, but sufficiently far away from the contact line the relative heights of the thin film are nearly identical.

Another advantage of the framework is practical, in that the computational time for these calculations is $O(\text{min})$ using the open-source oomph-lib framework with state-of-the-art linear algebra solvers, rather than $O(\text{days})$ for the MD simulations. As we are able to obtain the velocity and pressure fields in addition, this unified model has excellent potential for researchers wishing to combine the best aspects of the hydrodynamic and molecular theories in their work. We also remark that viscous and inertial effects can be incorporated in this model by, for example, treating the gas phase using a lubrication approximation; see Keeler *et al.* (2021). We also remark that the QP model and associated asymptotic results, while not resolving the flow field, are useful for validation, as demonstrated here.

Nevertheless, there remains a need for more physical experiments with emphasis on the RCL up to the point of film deposition, since, as we have seen, this encodes much valuable information concerning the contact angle on the microscopic scale. While there is a very large body of literature on film deposition, such as that which occurs when a solid surface is withdrawn from a pool of liquid, and much published data on advancing contact angles, comprehensive measurements of dynamic receding angles on partially wetted surfaces are, unfortunately, rare. A resurgence of interest is overdue.

Declaration of interests. The authors report no conflict of interest.

Author ORCIDs.
- J.S. Keeler https://orcid.org/0000-0002-8653-7970;
- T.D. Blake https://orcid.org/0000-0002-7547-8522;
- D.A. Lockerby https://orcid.org/0000-0001-5232-7986;
- J.E. Sprittles https://orcid.org/0000-0002-4169-6468.

Author contributions. J.S.K. performed the theoretical analysis pertaining to the continuum model and numerical simulations. T.D.B. wrote the appendix on the MKT theory. All authors contributed equally to analysing data, reaching conclusions and writing the paper.

Appendix A. Molecular-kinetic theory

According to the MKT of dynamic wetting, the contact line advances or recedes across the energy landscape of the solid surface as a consequence of random, thermally activated molecular events having characteristic frequency κ_0^* and length λ_0^* (not to be confused with the dimensionless slip length λ) (Blake & Haynes 1967; Blake 1993). Such events occur across the whole solid–liquid interface, but only those that take place within the TPZ determine dynamic wetting. The TPZ, of width δ^*, is the region where the liquid–vapour and solid–liquid interfaces meet, i.e. the contact line viewed at the molecular scale. At equilibrium, the molecular events simply cause the contact line to fluctuate about its mean position (Fernández-Toledano, Blake & De Coninck 2019, 2020a; Fernández-Toledano *et al.* 2020b). However, for net displacement of the contact line at velocity U_{cl}^*, work must be done to favour events in the desired direction. This work is provided by the out-of-balance surface tension force that arises when the equilibrium is disturbed: $f^* = \gamma_L^*(\cos(\theta_0) - \cos(\theta_{cl}))$, where γ_L^* is the surface tension of the liquid. According to the model, as the TPZ moves across the solid surface, this work is expended at n^* interaction sites per unit area swept. Application of the Frenkel–Eyring theory of stress-modified activated rate processes (Glasstone, Laidler & Eyring 1941; Frenkel 1946) then leads to the principal equation linking U_{cl}^* and θ_{cl},

$$U_{cl}^* = 2\kappa_0^*\lambda_0^* \sinh\left[\gamma_L^* \left(\cos(\theta_0) - \cos(\theta_{cl})\right)/2n^*k_BT\right], \tag{A1}$$

where k_B and T are, respectively, the Boltzmann constant and the absolute temperature.

Since its inception, this equation has proved very effective in correlating experimental and MD data for a wide range of systems; see, for example, Blake (1993), Schneemilch *et al.* (1998), Blake (2006) and Duvivier, Blake & De Coninck (2013). In the interpretation of experimental data, the interaction sites are usually assumed to be uniformly distributed, so that $\lambda_0^* \approx 1/\sqrt{n^*}$; thus reducing the unknowns to just two: κ_0^* and λ_0^*.

For small arguments of sinh, typically when θ_{cl} is not too far from θ_0 (true for θ_{cl} at the RCL in the MD data investigated here) or γ_L^* is small, this reduces to a linear relationship

$$U_{cl}^* = \left(\frac{\kappa_0^*\lambda_0^*}{n^*k_BT}\right) \gamma_L^* \left(\cos(\theta_0) - \cos(\theta_{cl})\right), \tag{A2}$$

which may be written as

$$Ca_{cl} = \frac{\mu_L^*}{\zeta^*} \left(\cos(\theta_0) - \cos(\theta_{cl})\right), \tag{A3}$$

where ζ^* is the coefficient of contact line friction (per unit length of the contact line),

$$\zeta^* = \frac{n^* k_B T}{\kappa_0^* \lambda_0^*}. \tag{A4}$$

This single coefficient quantifies the localised resistance to the displacement of the contact line.

In previous MD studies (Bertrand, Blake & De Coninck 2009; Blake *et al.* 2015) it has been shown that both contact line friction and slip between a liquid and a solid depend on the same thermally activated molecular events. Whereas, at the contact line, the principle driving force comes from the out-of-balance surface tension acting across the TPZ, for the latter, it is provided by the viscous shear stress acting across the whole solid–liquid interface: $\mu_L^*(\partial u^*/\partial z^*) = \beta^* \lambda^*$, where β^* is the slip coefficient and λ^* the Navier-slip length (i.e. the distance into the solid at which the extrapolated fluid velocity vanishes). Because of the common mechanism, it follows that the two coefficients are directly related; specifically,

$$\beta^* = \zeta^*/\delta^*; \tag{A5}$$

hence,

$$\lambda^* = \delta^* \mu_L^*/\zeta^*. \tag{A6}$$

This relationship has been validated by MD simulations, in which both the contact line friction and the slip length have been measured for the same system over a range of equilibrium contact angles (Blake *et al.* 2015; Fernández-Toledano *et al.* 2020*b*). Good agreement has been shown for both Lennard–Jones liquids and atomistically simulated water on molecularly smooth carbon-like surfaces. That said, a precise correlation hinges on the value of δ^*. For the Lennard–Jones liquids, the value selected was assessed from the velocity profiles across the TPZ. For the simulated water system, the distance over which the density of the liquid in contact with the solid fell to zero was used. See figure 10 in Blake *et al.* (2015) to compare the two approaches. Arguments may be made for both. For the Lennard–Jones system, the difference in the result was in the region of 30 %. Slip lengths were smaller if the density profile was used. In addition, the value of δ^* appeared to depend weakly on both contact line velocity and the equilibrium contact angle. Based on the existing data, while (A6) appears to be physically justified, a precise understanding of the subtle influences in play requires more work. The value of δ^* found for the coarse-grained water simulations (Fernández-Toledano *et al.* 2021) was 0.93 ± 0.14 nm based on the density argument. We use this value in the present paper.

If (A6) is accepted, at least in principle, it allows us to rewrite (A3) in dimensionless variables, as

$$Ca_{cl} = \frac{\lambda}{\delta} \left(\cos(\theta_0) - \cos(\theta_{cl}) \right). \tag{A7}$$

In the stationary frame of the liquid plug between two solid walls moving at velocity U_{wall}^*, this becomes

$$Ca \left(U_{wall} - \frac{\partial x_{cl}}{\partial t} \right) = \frac{\lambda}{\delta} \left(\cos(\theta_0) - \cos(\theta_{cl}) \right), \tag{A8}$$

which is (2.11) in the main body of the paper when we set the non-dimensional wall speed to be $U_{wall} = -1$. Furthermore, and perhaps more significantly, we know that contact line friction depends strongly on the equilibrium contact angle. This means that the same is true for the slip length. As has been shown by Blake (1993), Blake & De Coninck (2002),

Bertrand *et al.* (2009), Duvivier *et al.* (2013), the frequency κ_0^* is related to the equilibrium contact angle by

$$\kappa_0^* \sim \left(k_B T/\mu_L^* v_L^*\right) \exp\left[-\gamma_L^* \left(1 + \cos(\theta_0)\right)/n^* k_B T\right], \tag{A9}$$

where v_L^* is the molecular flow volume in the Frenkel–Eyring theory. This leads to

$$\zeta^* \sim \left(n^* \mu_L^* v_L^*/\lambda_0^*\right) \exp\left[-\gamma_L^* \left(1 + \cos(\theta_0)\right)/n^* k_B T\right] \tag{A10}$$

and, hence, to

$$\lambda^* \sim \delta^* \left(\lambda_0^*/n^* v_L^*\right) \exp\left[-\gamma_L^* \left(1 + \cos(\theta_0)\right)/n^* k_B T\right]. \tag{A11}$$

This suggests the general (dimensionless) form

$$\lambda = a \exp\left[b(1 + \cos(\theta_0)\right]. \tag{A12}$$

In the present paper we have used this expression, (2.13), to fit the slip length calculated from the MD data in table 1 of Fernández-Toledano *et al.* (2021).

REFERENCES

AFKHAMI, S., GAMBARYAN-ROISMAN, T. & PISMEN, L.M. 2020 Challenges in nanoscale physics of wetting phenomena. *Euro. Phys. J.* **229** (10), 1735–1738.

ANDREOTTI, B. & SNOEIJER, J.H. 2020 Statics and dynamics of soft wetting. *Annu. Rev. Fluid Mech.* **52**, 285–308.

BARRAT, J-L. & BOCQUET, L. 1999 Influence of wetting properties on hydrodynamic boundary conditions at a fluid/solid interface. *Faraday Discuss.* **112**, 119–128.

BARTHLOTT, W., MAIL, M. & NEINHUIS, C. 2016 Superhydrophobic hierarchically structured surfaces in biology: evolution, structural principles and biomimetic applications. *Phil. Trans. R. Soc. Lond.* A **374** (2073), p. 20160191.

BEATTY, S.M. & SMITH, J.E. 2010 Fractional wettability and contact angle dynamics in burned water repellent soils. *J. Hydrol.* **391** (1–2), 97–108.

BERTRAND, E., BLAKE, T.D. & DE CONINCK, J. 2009 Influence of solid-liquid interactions on dynamic wetting: a molecular dynamics study. *J. Phys.: Condens. Matter* **21**, 464124.

BLAKE, T.D. 1993 Dynamic contact angles and wetting kinetics. In *Wettability* (ed. J.C. Berg), pp. 251–309. Marcel Dekker.

BLAKE, T.D. 2006 The physics of moving wetting lines. *J. Colloid Interface Sci.* **299**, 1–13.

BLAKE, T.D. & DE CONINCK, J. 2002 The influence of solid/liquid interactions on dynamic wetting. *Adv. Colloid Interface Sci.* **96**, 21–36.

BLAKE, T.D. & HAYNES, J.M 1967 Kinetics of liquid/liquid displacement. *J. Colloid Interface Sci.* **14**, 421–423.

BLAKE, T.D & RUSCHAK, K.J. 1979 A maximum speed of wetting. *Nature* **282**, 489–491.

BLAKE, T.D., FERNÁNDEZ TOLEDANO, J.C., DOYEN, G. & DE CONINCK, J. 2015 Forced wetting and hydrodynamic assist. *Phys. Fluids* **27**, 11210.

BROCHARD-WYART, F. & DE GENNES, P.G. 1992 Dynamics of partial wetting. *Adv. Colloid Interface Sci.* **39**, 1–11.

CHAN, T.S., SNOEIJER, J.H. & EGGERS, J. 2012 Theory of the forced wetting transition. *Phys. Fluids* **24**, 072104.

CHEN, L., YU, J. & WANG, H. 2014 Convex nanobending at a moving contact line: the missing mesoscopic link in dynamic wetting. *ACS Nano* **8**, 11493.

CHEN, Q., RAMÉ, E. & GAROFF, S. 1995 The breakdown of asymptotic hydrodynamic models of liquid spreading at increasing capillary number. *Phys. Fluids* **7**, 2631–2639.

COX, R.G. 1986 The dynamics of the spreading of liquids on a solid surface. Part 1. Viscous flow. *J. Fluid Mech.* **168**, 169–194

DE CONINCK, J. & BLAKE, T.D. 2008 Wetting and molecular dynamics simulations of simple liquids. *Annu. Rev. Mater. Res.* **38**, 1–22.

DE GENNES, P.-G. 1985 Wetting: statics and dynamics. *Rev. Mod. Phys.* **57** (3), 827.

DERYAGUIN, B.V. 1943 On the thickness of a layer of liquid remaining on the walls of vessels after their emptying, and the theory of the application of photoemulsion after coating on the cine film. *Acta Physicochim. USSR* **20**, 349.

DODDS, S., CARVALHO, M.S. & KUMAR, S. 2012 The dynamics of three-dimensional liquid bridges with pinned and moving contact lines. *J. Fluid Mech.* **707**, 521–540.

DUSSAN, V.E.B. 1979 On the spreading of liquids on solid surfaces: static and dynamic contact lines. *Annu. Rev. Fluid Mech.* **11**, 371–400.

DUVIVIER, D., BLAKE, T.D. & DE CONINCK, J. 2013 Towards a predictive theory of wetting dynamics. *Langmuir* **29**, 10132–10140.

EGGERS, J. 2004 Hydrodynamic theory of forced dewetting. *Phys. Rev. Lett.* **96**, 174504.

EGGERS, J. 2005 Existence of receding and advancing contact lines. *Phys. Fluids* **17**, 082106.

FERNÁNDEZ-TOLEDANO, J.C., BLAKE, T.D. & DE CONINCK, J. 2019 Contact-line fluctuations and dynamic wetting. *J. Colloid Interface Sci.* **540**, 322–329.

FERNÁNDEZ-TOLEDANO, J.C., BLAKE, T.D. & DE CONINCK, J. 2020*a* Moving contact lines and Langevin formalism. *J. Colloid Interface Sci.* **562**, 287–292.

FERNÁNDEZ-TOLEDANO, J.C., BLAKE, T.D. & DE CONINCK, J.D. 2020*b* The hidden microscopic life of the moving contact line of a waterlike liquid. *Phys. Rev. Fluids* **5**, 104004.

FERNÁNDEZ-TOLEDANO, J.C., BLAKE, T.D. & DE CONINCK, J.D. 2021 Taking a closer look: a molecular-dynamics investigation of microscopic and apparent dynamic contact angles. *J. Colloid Interface Sci.* **587**, 311–323.

FLITTON, J.C. & KING, J.R. 2004 Surface-tension-driven dewetting of Newtonian and power-law fluids. *J. Engng Maths* **50** (2–3), 241–266.

FRENKEL, J.I. 1946 *Kinetic Theory of Liquids*. Oxford University Press.

DE GENNES, P.G. 1986 Deposition of Langmuir–Blodgett layers. *Colloid Polym. Sci.* **264**, 463–465.

GERRITSEN, M.G. & DURLOFSKY, L.G. 2005 Modelling fluid flow in oil reservoirs. *Annu. Rev. Fluid Mech.* **37** (1), 211–238.

GLASSTONE, S., LAIDLER, K.J. & EYRING, H. 1941 *The Theory of Rate Processes*. McGraw-Hill.

HADJICONSTANTINOU, N.G. 1999 Hybrid atomistic–continuum formulations and the moving contact-line problem. *J. Comput. Phys.* **154** (2), 245–265.

HEIL, M. & HAZEL, A.L. 2006 oomph-lib – An object-oriented multi-physics finite-element library. In *Fluid-Structure Interaction* (ed. H.-J. Bungatz & M. Schäfer), pp. 19–49. Springer.

HOFFMAN, R.L. 1975 A study of the advancing interface. I. Interface shape in liquid—gas systems. *J. Colloid Interface Sci.* **50** (2), 228–241.

HUH, C. & SCRIVEN, L.E. 1971 Hydrodynamic model of steady movement of a solid/liquid/fluid contact line. *J. Colloid Interface Sci.* **35** (1), 85–101.

JACQMIN, D. 2004 Onset of wetting failure in liquid–liquid systems. *J. Fluid Mech.* **517**, 209–228.

KAMAL, C., SPRITTLES, J.E., SNOEIJER, J.H. & EGGERS, J. 2019 Dynamic drying transition via free-surface cusps. *J. Fluid Mech.* **858**, 760–786.

KEELER, J., LOCKERBY, D., KUMAR, S. & SPRITTLES, J. 2021 Stability and bifurcation of dynamic contact lines in two dimensions. *J. Fluid Mech.* **945**, A34.

KOPLIK, J. & BANAVAR, J.R. 1995 Continuum deductions from molecular hydrodynamics. *Annu. Rev. Fluid Mech.* **27** (1), 257–292.

KREUTZER, M.T., SHAH, M.S., PARTHIBAN, P. & KHAN, S.A. 2018 Evolution of nonconformal Landau–Levich–Bretherton films of partially wetting liquids. *Phys. Rev. Fluids* **3** (1), 014203.

KUMAR, S. 2015 Liquid transfer in printing processes: liquid bridges with moving contact lines. *Annu. Rev. Fluid Mech.* **47**, 67–94.

LANDAU, L. & LEVICH, B. 1988 Dragging of a liquid by a moving plate. In *Dynamics of Curved Fronts*, pp. 141–153. Elsevier.

LHERMEROUT, R. & DAVITT, K. 2019 Contact angle dynamics on pseudo-brushes: effect of polymer chain length and wetting liquid. *Colloids Surf. (A)* **566**, 148–155.

LIU, C.-Y., CARVALHO, M.S. & KUMAR, S. 2017 Mechanisms of dynamic wetting failure in the presence of soluble surfactants. *J. Fluid Mech.* **825**, 677–703.

LIU, C.-Y., CARVALHO, M.S. & KUMAR, S. 2019 Dynamic wetting failure in curtain coating: comparison of model predictions and experimental observations. *Chem. Engng Sci.* **195**, 74–82.

LIU, C.-Y., VANDRE, E., CARVALHO, M.S. & KUMAR, S. 2016*a* Dynamic wetting failure and hydrodynamic assist in curtain coating. *J. Fluid Mech.* **808**, 290–315.

LIU, C.-Y., VANDRE, E., CARVALHO, M.S. & KUMAR, S. 2016*b* Dynamic wetting failure in surfactant solutions. *J. Fluid Mech.* **789**, 285–309.

LUKYANOV, A.V. & PRYER, T. 2017 Hydrodynamics of moving contact lines: macroscopic versus microscopic. *Langmuir* **33** (34), 8582–8590.

OMORI, T. & KAJISHIMA, T. 2017 Apparent and microscopic dynamic contact angles in confined flows. *Phys. Rev. Fluids* **29**, 112107.

PAPIEROWSKA, E., SZPORAK-WASILEWSKA, S., SZEWIŃSKA, J., SZATYŁOWICZ, J., DEBAENE, G. & UTRATNA, M. 2018 Contact angle measurements and water drop behavior on leaf surface for several deciduous shrub and tree species from a temperate zone. *Trees* **32** (5), 1253–1266.

PRIEZJEV, N.V. 2007 Rate-dependent slip boundary conditions for simple fluids. *Phys. Rev.* E **75** (5), 051605.

QIAN, T., WANG, X.-P. & SHENG, P. 2003 Molecular scale contact line hydrodynamics of immiscible flows. *Phys. Rev.* E **68** (1), 016306.

REDDY, S., SCHUNK, P.R. & BONNECAZE, R.T. 2005 Dynamics of low capillary number interfaces moving through sharp features. *Phys. Fluids* **17** (12), 122104.

REDON, C., BROCHARD-WYART, F. & RONELEZ, F. 1991 Dynamics of dewetting. *Phys. Rev. Lett.* **66**, 715–718.

REN, W. & WEINAN, E. 2007 Boundary conditions for the moving contact line problem. *Phys. Fluids* **19** (2), 022101.

REN, W., HU, D. & WEINAN, E. 2010 Continuum models for the contact line problem. *Phys. Fluids* **22** (10), 102103.

RIO, E., DAERR, A., ANDREOTTI, B. & LIMAT, L. 2005 Boundary conditions in the vicinity of a dynamic contact line: experimental investigation of viscous drops sliding down an inclined plane. *Phys. Rev. Lett.* **94**, 024503.

SBRAGAGLIA, M., SUGIYAMA, K. & BIFERALE, L. 2008 Wetting failure and contact line dynamics in a Couette flow. *J. Fluid Mech.* **614**, 471–493.

SCHNEEMILCH, M., HAYES, R.A., PETROV, J.G. & RALSTON, J. 1998 Dynamic wetting and dewetting of a low-energy surface by pure liquids. *Langmuir* **14**, 7047–7051.

SEMENOV, S., STAROV, V.M., VELARDE, M.G. & RUBIO, R.G. 2011 Droplets evaporation: problems and solutions. *Eur. Phys. J.* **197** (1), 265–278.

SHIKHMURZAEV, Y.D. 2007 *Capillary Flows with Forming Interfaces*. CRC.

SNOEIJER, J.H. 2006 Free-surface flows with large slopes: beyond lubrication theory. *Phys. Fluids* **18** (2), 021701.

SNOEIJER, J.H. & ANDREOTTI, B. 2013 Moving contact lines: scales, regimes, and dynamical transitions. *Annu. Rev. Fluid. Mech.* **45**, 269–292.

SNOEIJER, J.H., ANDREOTTI, B., DELON, G. & FERMIGIER, M. 2007 Relaxation of a dewetting contact line. Part 1. A full-scale hydrodynamic calculation. *J. Fluid. Mech.* **579**, 63–83.

SNOEIJER, J.H., DELON, G., ANDREOTTI, B. & FERMIGIER, M. 2006 Avoided critical behavior in dynamically forced wetting. *Phys. Rev. Lett.* **96**, 174504.

SNOEIJER, J.H., ZIEGLER, J., ANDREOTTI, B., FERMIGIER, M. & EGGERS, J. 2008 Thick films of viscous fluid coating a plate withdrawn from a liquid reservoir. *Phys. Rev. Lett.* **100** (24), 244502.

SPRITTLES, J.E. & SHIKHMURZAEV, Y.D. 2011*a* Viscous flow in domains with corners: numerical artifacts, their origin and removal. *Comput. Meth. Appl. Mech. Engng* **200** (9–12), 1087–1099.

SPRITTLES, J.E. & SHIKHMURZAEV, Y.D. 2011*b* Viscous flows in corner regions: singularities and hidden eigensolutions. *Intl J. Numer. Meth. Fluids* **65** (4), 372–382.

SPRITTLES, J.E. & SHIKHMURZAEV, Y.D. 2012 Finite element framework for describing dynamic wetting phenomena. *Intl J. Numer. Meth. Fluids* **68** (10), 1257–1298.

SPRITTLES, J.E. & SHIKHMURZAEV, Y.D. 2013 Finite element simulation of dynamic wetting flows as an interface formation process. *J. Comput. Phys.* **233**, 34–65.

STONE, H.A., STROOCK, A.D. & AJDARI, A. 2004 Engineering flows in small devices: microfluidics toward a lab-on-a-chip. *Annu. Rev. Fluid Mech.* **36** (1), 381–411.

SUI, Y., DING, H. & SPELT, P.D.M. 2014 Numerical simulations of flows with moving contact lines. *Annu. Rev. Fluid Mech.* **46**, 97–119.

TOLSTOI, D.M. 1952 Molecular theory of slip over solid surfaces. *Dokl. Akad. Nauk SSSR* **85**, 1089–1092.

VANDRE, E. 2013 Onset of dynamic wetting failure: the mechanics of high-speed fluid displacement. PhD thesis, University of Minnesota, USA.

VANDRE, E., CARVALHO, M.S. & KUMAR, S. 2012 Delaying the onset of dynamic wetting failure through meniscus confinement. *J. Fluid Mech.* **707**, 496–520.

VANDRE, E., CARVALHO, M.S. & KUMAR, S. 2013 On the mechanism of wetting failure during fluid displacement along a moving substrate. *Phys. Fluids* **25**, 102103.

VOINOV, O.V. 1976 Hydrodynamics of wetting. *Fluid Dyn.* **11**, 714–721.

WEINSTEIN, S.J. & RUSCHAK, K.J. 2004 Coating flows. *Annu. Rev. Fluid Mech.* **36** (1), 29–53.

WILSON, M.C.T, SUMMERS, J.L., SHIKHMURZAEV, Y.D., CLARKE, A. & BLAKE, T.D. 2006 Nonlocal hydrodynamic influence on the dynamic contact angle: slip models versus experiment. *Phys. Rev.* E **73** (4), 041606.

XU, J.-J. & REN, W. 2014 A level-set method for two-phase flows with moving contact line and insoluble surfactant. *J. Comput. Phys.* **263**, 71–90.

YUE, P. & FENG, J.J. 2011 Wall energy relaxation in the Cahn–Hilliard model for moving contact lines. *Phys. Fluids* **23** (1), 012106.

ZHAO, B., PAHLAVAN, A.A., CUETO-FELGUEROSO, L. & JUANES, R. 2018 Forced wetting transition and bubble pinch-off in a capillary tube. *Phys. Rev. Lett.* **120** (8), 084501.

ZIENKIEWICZ, O.C. & ZHU, J.Z. 1992 The superconvergent patch recovery and a posteriori error estimates. Part 1: the recovery technique. *Intl J. Numer. Meth. Engng* **33** (7), 1331–1364.